

Grand canonical finite size numerical approaches in one and two dimensions: Real space energy renormalization and edge state generation

Chisa Hotta,¹ Satoshi Nishimoto,² and Naokazu Shibata³¹*Department of Physics, Kyoto Sangyo University, Kyoto 603-8555, Japan*²*Institute for Theoretical Solid State Physics, IFW Dresden, 01171 Dresden, Germany*³*Department of Physics, Tohoku University, Sendai 980-8578, Japan*

(Received 2 December 2012; published 21 March 2013)

The grand canonical numerical analysis recently developed for quantum many-body systems on a finite cluster [C. Hotta and N. Shibata, *Phys. Rev. B* **86**, 041108(R) (2012)] is the technique to efficiently obtain the physical quantities in an applied field. There, the observables are the continuous and real functions of fields, mimicking their thermodynamic limit, even when a small cluster is adopted. We develop a theory to explain the mechanism of this analysis based on the deformation of the Hamiltonian. The deformation spatially scales down the energy unit from the system center toward zero at the open edge sites, which introduces the renormalization of the energy levels in a way reminiscent of Wilson's numerical renormalization group. However, compared to Wilson's case, our deformation generates a number of far well-localized edge states near the chemical potential level, which are connected via a very small quantum fluctuation in k space with the "bulk" states which spread at the center of the system. As a response to the applied field, the particles on the cluster are self-organized to tune the particle number of the bulk states to their thermodynamic limit by using the "edges" as a buffer. We demonstrate the present analysis in two-dimensional quantum spin systems on square and triangular lattices, and determine the smooth magnetization curve with a clear $\frac{1}{3}$ plateau structure in the latter.

DOI: [10.1103/PhysRevB.87.115128](https://doi.org/10.1103/PhysRevB.87.115128)

PACS number(s): 02.60.-x, 71.27.+a, 71.10.-w

I. INTRODUCTION

Solving quantum many-body problems in solids basically aims to understand the physical properties in the bulk. Most of the solvers nowadays are numerics, e.g., molecular dynamics, Monte Carlo simulation, exact diagonalization, etc., where the standard procedure to reach the thermodynamic limit is the finite size scaling. Although the bulk physical quantities determined by the scaling analysis are, in principle, independent of the boundary conditions, the finite size corrections sometimes strongly depend on the types of boundaries imposed.

There are mainly three explicit problems the boundary conditions possess. One is the unphysical discreteness of the quantum numbers. For example, if one calculates the energy dispersion, the wave number is given in a series of rational numbers n/L , with the integer number n against the system size L . Resultantly, only a discrete spectrum is obtained even after the size scaling. The second problem is the lack of methodology to connect the system and the bath via ideally small fluctuations when one wants to determine the low-energy excitations or response functions to weak fields. The last problem arises when we adopt the open boundary condition (OBC); the open edges behave as impurities and induce a Friedel oscillation, in which case, the states which have different symmetry from the original target state rumple the results, particularly when the system size is not large enough against the dominant correlation length.¹ This artifact is called the "boundary effect."

Now, the states which are trapped at the open edges are called "edge states." While in some cases the edge states have achieved physical meaning of their own,² they are so often the cause of the boundary effect, which should be eliminated. If one could efficiently separate the edge state with the bulk and could further control the connection between them, the edge states could be used with advantage.

Some of the authors recently developed a numerical scheme called "grand canonical analysis,"³ which enables us to effectively separate the quantization process of quantum mechanics and the boundary conditions, resolving all the above problems. One could observe directly the physical quantities, mimicking their thermodynamic limit at small and fixed finite sizes, free of boundary effect or of finite size effect. The observables and quantum numbers are then the continuous functions of applied fields.

The key ingredient of this analysis is to deform the Hamiltonian in real space. In usual boundary conditions, the wave number k is discretized in equal spacing as, e.g., $2\pi n/L$ (n : integer), which gives approximately the equally spaced energy levels, and the Fermi level feels this discretization. By contrast, the deformation could systematically generate the dense low-energy levels in analogy to Wilson's numerical renormalization group (NRG).⁴ Wilson's NRG increased the system size one by one while renormalizing the energy scale each time to reach a scale-free fixed point. Whereas, we fix the system size and force the renormalization of the energy scale by hand via gradually varying deformation function. This also attains the scale-free quantities. Further, the low-energy quasiparticle excited states thus generated are well localized on edges due to heavy mass, and serve as a buffer to absorb/release the excess/deficient (quasi)particles with a lighter mass in the main part of the system. Such scale-free character and the generation of localized edge states as a "particle bath" together enable the grand canonical self-tuning and realize the optimized "bulk" state in the finite size cluster.

This paper provides the detailed mechanism of the scheme we mentioned above and shows wide applications to two-dimensional (2D) lattice models. The paper is organized as follows. In Sec. II, the grand canonical analysis is briefly reviewed. In Sec. III, its mechanism is explained based

on the noninteracting one-dimensional (1D) systems. The connections to Wilson's renormalization group are given in Sec. IV. Then, Sec. V provides the representative examples of the 1D and 2D quantum many-body lattice models in which we use the density-matrix renormalization group (DMRG) method⁵ as a solver. Particularly, *the bulk magnetization curve* of the triangular lattice antiferromagnet, which is no longer a staircase of a finite size, but *a true curve*, is obtained within reasonable numerical cost. We finalize the paper in Sec. VI with some discussions and conclusions. The applicability to the gapped systems and the feasibility of the type of deformation function are given in the Appendixes. Those who are not interested in the structure of the scheme could skip Secs. III and IV and straightforwardly go through the methodology and examples given in Secs. II and V, respectively.

II. GRAND CANONICAL ANALYSIS

We first give a brief explanation of the grand canonical analysis invented in Ref. 3 by generalizing it to those including not only 1D but 2D and different lattice structures. Consider the Hamiltonian consisting of N sites with some open ends,

$$\mathcal{H} = \sum_{i=1}^N u(i) + \sum_{\langle i,j \rangle} h_l(i,j), \quad (1)$$

where $u(i)$ denotes the onsite interaction and potential terms, and $h_l(i,j)$ is the interaction term between i th and j th sites of distance $l = |i - j|$. This original Hamiltonian is deformed as

$$\mathcal{H}_{\text{deform}} = \sum_{i=1}^N f(\mathbf{r}_i)u(i) + \sum_{\langle i,j \rangle} f\left(\frac{\mathbf{r}_i + \mathbf{r}_j}{2}\right)h_l(i,j). \quad (2)$$

Here, $f(\mathbf{r})$ is the externally given function, which should smoothly vary from the maximum value at the center of the finite cluster to zero at the edges. For such function, we mainly adopt the so-called sine-square deformation (SSD) function, first introduced as the most optimal smooth boundary condition by Gendiar, Daniska, Lee, and Nishino.⁶ For the 1D chain, the SSD function for the i th site ($\mathbf{r}_i = i$) is given as

$$f_{\text{SSD}}(i) = \sin^2 \left[\frac{\pi}{L} \left(i - \frac{1}{2} \right) \right], \quad i = 1 \sim L. \quad (3)$$

As for the 2D systems, there are many different types of lattice geometry as well as shape of the cluster. As the representative examples among them, we choose a series of clusters in units of square and triangle shown in Figs. 1(b)–1(e), with a total number of sites N (N is varied by uniformly expanding the clusters). The deformation on such clusters can be done in three ways in 2D. In the long cylinder shown in Fig. 1(b), the deformation is given along the leg as in 1D. For the other 2D clusters in Figs. 1(c)–1(e), it could be given along the Cartesian and polar coordinates, the origins of which are placed at the center of the clusters. For example, the Cartesian deformation for a square lattice with $\mathbf{r} = (x, y)$ is given as

$$f(x, y) = \frac{1}{4} \left[1 + \cos \left(\frac{\pi x}{L_x} \right) \right] \left[1 + \cos \left(\frac{\pi y}{L_y} \right) \right]. \quad (4)$$

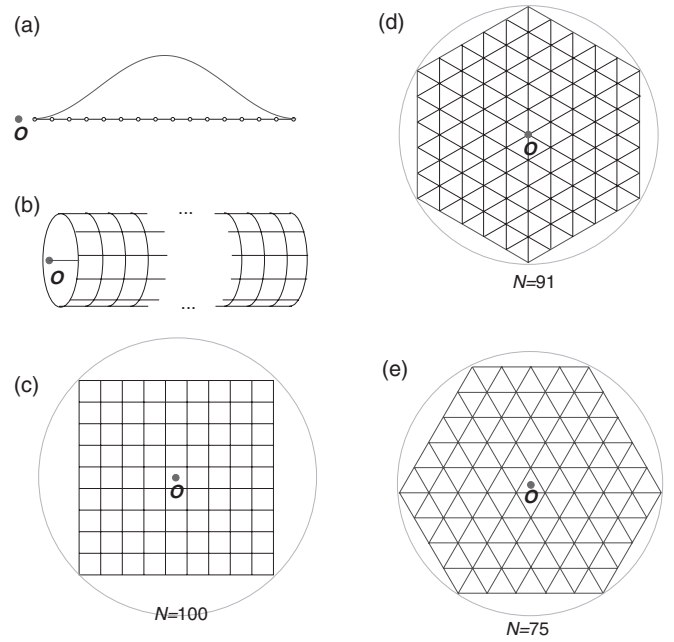


FIG. 1. Examples of finite size clusters used in the grand canonical analysis. (a) 1D chain, (b) long cylinder with periodic boundary in the circumference direction, and 2D clusters, (c) square lattice, (d) triangular lattice on a hexagonal cluster, and (e) triangular lattice on an irregular hexagonal cluster. One can develop a series (d) $N = 37, 61, 91, 127, 169$ and (e) $N = 27, 48, 75, 97, 147$ by uniformly expanding the cluster. Origin of the clusters is marked with a circle, and the large circle corresponds to the range of radius R , used in Eq. (5).

If we adopt the hexagonal cluster, the similar deformation is constructed as a product of the SSD functions running along the three bond directions. As for the polar coordinate $\mathbf{r} = (r, \theta)$, we define

$$f(r) = \frac{1}{2} \left[1 + \cos \left(\frac{\pi r}{R} \right) \right]. \quad (5)$$

The radius R is chosen so as to nearly exactly cover the whole cluster as indicated by circles in Figs. 1(c)–1(e). In Ref. 3, we showed that any smoothly varying function, as far as it is convex downward at the edges, could be applied as $f(\mathbf{r})$. However, in this section, we concentrate on the above SSDs. The other types of deformation are discussed in Sec. IV and Appendix B. There, the SSD turns out to be the optimal deformation function for the grand canonical analysis.

The main purpose of the present procedure is to measure the number of “particles” for a given external conjugate field; the number of magnons (magnetization or hard-core bosons) for an external magnetic field h in the quantum magnets, and the electron number for a given chemical potential μ in the electronic systems. The Zeeman term $-hf(\mathbf{r}_i)S_i^z$ and the chemical potential term $-\mu f(\mathbf{r}_i)n_i$ are deformed as the onsite term of Eq. (2). In the electronic system, $E = \langle \mathcal{H} \rangle$ including the chemical potential term corresponds to the thermodynamic potential at zero temperature.

The total particle number of the whole system is a conserved number, which is given by hand as some integer number M_g or N_g . After diagonalizing Eq. (2) including these field terms,

one finds that the wave functions are no longer translationally invariant, but the relations

$$M_g = \sum_{i=1}^N \langle S_i^z \rangle \quad (6)$$

in quantum magnets and

$$N_g = \sum_{i=1}^N \langle n_i \rangle \quad (7)$$

in the electronic system always hold. In the translationally invariant system such as the one with periodic boundary conditions (PBC), $\langle S_i^z \rangle$ and $\langle n_i \rangle$ are spatially uniform quantities, corresponding to M_g/N and N_g/N , respectively. However, by the deformation, the spatial variation of $\langle S_i^z \rangle$ and $\langle n_i \rangle$ arises in the specific manner as we show in the following.

In going further, we adopt the simplest example, the 1D tight-binding model of noninteracting fermions, the Hamiltonian of which is given as

$$\mathcal{H}_0 = - \sum_{j=1}^L (c_j^\dagger c_{j+1} + \text{H.c.}) - \mu \sum_{j=1}^L n_j, \quad (8)$$

where c_j^\dagger/c_j denotes the creation/annihilation operator of fermions on the j th site, and $n_j = c_j^\dagger c_j$ is the number operator. We now deform the Hamiltonian as

$$\mathcal{H}_{\text{deform}} = - \sum_{j=1}^{L-1} f\left(j + \frac{1}{2}\right) (c_j^\dagger c_{j+1} + \text{H.c.}) - \mu \sum_{j=1}^L f(j) n_j \quad (9)$$

by the deformation function $f(j) = f_{\text{SSD}}(j)$ in Eq. (3). After diagonalizing Eq. (9), one obtains the L -different one-body eigenstates $\varphi_l(j)$ ($l = 1 \sim L$). By filling these states from the lowest energy with N_g particles, the wave function $|\Phi_g\rangle = \prod_{l=1}^{N_g} (\sum_{j=1}^L \varphi_l^*(j) c_j^\dagger) |0\rangle$ is obtained, where $|0\rangle$ denotes the vacuum.

Figure 2(a) shows the spatial profile of the expectation value of $\langle n_i \rangle = \sum_{l=1}^{N_g} |\varphi_l(i)|^2$ for several choices of N_g . One finds that the variation of N_g mainly affects $\langle n_i \rangle$ on the edges, but those away from the edges do not change much. Here, note that there exists a small oscillation of a period of few sites, but the center of oscillation forms a smooth and slowly varying function. In order to extract the value of the oscillation center at around $i \sim L/2$, we take the average of $\langle n_i \rangle$ from the center of the system over $2r$ sites as

$$O(r) = \frac{1}{2r} \sum_{i=-r}^{r-1} \langle n_{i+\frac{L}{2}} \rangle. \quad (10)$$

As for the 2D system, the same operation is given by taking the average within the range of a circle of radius r from the center. As shown in Fig. 2(b), by plotting $O(r)$ as a function of r and by fitting them in powers of r as

$$O(r) = n_e + cr^2, \quad (11)$$

we obtain the oscillation center n_e . The extracted n_e measured from the exact bulk value $n_{\text{exact}} = 0.6666$ at $\mu = 1$ is plotted in Fig. 2(c) as a function of N_g/L for several choices of L . There

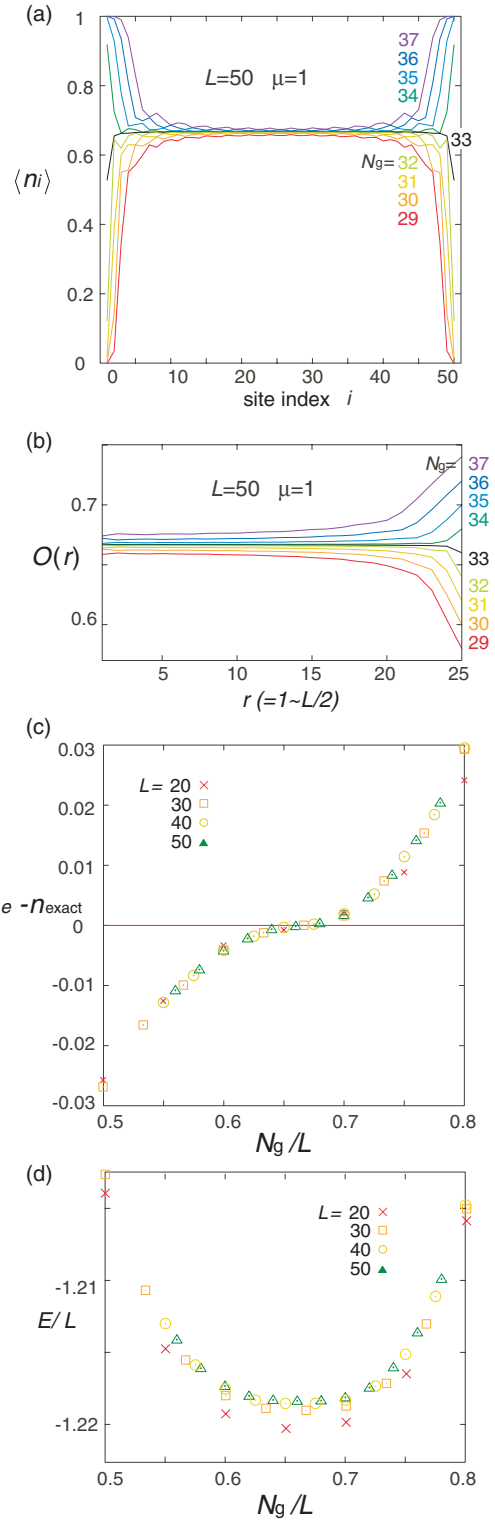


FIG. 2. (Color online) Grand canonical analysis on the tight-binding fermions at $\mu = 1$ on a $L = 50$ chain. (a) Spatial distribution of the particle density $\langle n_i \rangle$ for several choices of N_g . (b) $O(r)$ in Eq. (10) obtained from (a). (c) n_e obtained by the fit in Eq. (11) measured from $n_{\text{exact}} = 0.6666 \dots$ as a function of N_g/L . (d) Energy (thermodynamic potential) E/L corresponding to (c).

exists an inflection point at $n_e \sim n_{\text{exact}}$, which remains almost unchanged with L . This inflection point gives the most precise

result. The total energy (thermodynamic potential) E divided by L of the corresponding data is shown together in Fig. 2(d), where one finds that the inflection point of n_e corresponds to the local minimum of the energy.

In 1D, the range near the inflection point that fulfills the accuracy of $|n_e - n_{\text{exact}}| \lesssim 10^{-3}$ is $\Delta N_g/L \sim 0.05$. Therefore, even a rough estimate of N_g will give an accurate enough result. Note that in some strongly correlated 2D models with several competing local energy minimums, one needs to search for the optimal N_g to capture the proper ground state with the lowest energy, particularly when the available system length is not large enough.

Since the inflection point of error in Fig. 2(c) corresponds to the local energy minimum in Fig. 2(d), one expects that the present analysis follows the variational principle. Indeed, even for the interacting system, one could obtain the accurate expectation value mimicking its thermodynamic limit by the DMRG, one of the variational methods, within the typical error of 10^{-4} . We show in Sec. V the actual examples of such interacting systems.

We have previously interpreted these phenomena as a grand canonical ensemble in quantum mechanics.³ If the number of a given particle is larger than the optimal value, the excess “particles” spill out from the center of the system and accumulate at the edge sites. Or, when the particle number is smaller, the particles are unplugged from the edges to compensate for the loss at the center of the system. The edge sites have the measure zero energy, thus they do not contribute to the total energy, and could be approximately regarded as a buffer to adopt the center of the system to the optimal state. Why this happens is explained in more detail in Sec. III.

III. FORMULATION

A. Deformed Hamiltonian in reciprocal space

In this section, we explain how the deformation works to facilitate the grand canonical mechanism we saw in the previous section. For a moment, we continue concentrating on the noninteracting spinless fermions. Let us rewrite the Hamiltonian of Eq. (8) in reciprocal space as

$$\mathcal{H}_0 = \sum_k \epsilon(k) c_k^\dagger c_k, \quad (12)$$

with the energy dispersion $\epsilon(k) = -2 \cos k - \mu$. We impose the PBC, and the wave number is taken as $k = \delta n$ (n : integer), with $\delta = 2\pi/L$. The k th one-particle eigenstate is given as $c_k^\dagger |0\rangle$.

Next, we move on to the deformed Hamiltonian (2). For convenience, we redefine the deformation function (not restricted to SSD) as

$$f(j) = 1 - g(j). \quad (13)$$

Here, we set $g(j)$ as the periodic function in the range of $[\frac{1}{2} : L + \frac{1}{2}]$, which satisfies $|g(j)| = |g(L + 1 - j)|$. By expanding the function in terms of Fourier series as

$$g(j) = \sum_{n=-\infty}^{\infty} \hat{g}_n e^{i\delta n j}, \quad (14)$$

the deformed Hamiltonian in reciprocal space is obtained in the form

$$\begin{aligned} \mathcal{H}_{\text{deform}} &= \mathcal{H}_0 - \mathcal{H}_d, \\ \mathcal{H}_d &= \sum_k \sum_n \hat{g}_n \epsilon\left(k + \frac{\delta n}{2}\right) c_{k+\delta n}^\dagger c_k. \end{aligned} \quad (15)$$

One could recognize that the role of deformation is to introduce the mixing between the eigenstates of \mathcal{H}_0 . Originally, the wave number k was a good quantum number of \mathcal{H}_0 , but due to the finite mixing between k and $(k + \delta n)$ eigenstates, it is no longer a good quantum number of $\mathcal{H}_{\text{deform}}$. While the degree and the structure (δn) of the mixing depend on $\hat{g}(k)$, there is a common and important feature: $\epsilon(k + \frac{\delta n}{2})$ determines the mixing amplitude, which means that if there should exist some wave number k_0 that satisfies $\epsilon(k_0 + \frac{\delta n}{2}) = 0$, the mixing between the manifolds $\epsilon(k) > 0$ and $\epsilon(k) < 0$, which are separated at around k_0 , is suppressed.

B. SSD and PBC

The formulation in Sec. III A is basically the generalization of Maruyama *et al.*⁷ on the sine-square-deformation (SSD) in Eq. (3).⁸ They showed that the ground-state wave function \mathcal{H}_{SSD} coincides with the ground state of \mathcal{H}_0 with PBC if the chemical potential is properly chosen; let us consider the Fermi sea eigenwave function of Eq. (8) with PBC, $|\Psi_{\text{PBC}}\rangle = \prod_{|k| \leq k_g} c_k^\dagger |0\rangle$, by filling the N_g levels at $|k| \leq k_g$. Usually, this wave function is not the eigenstate of \mathcal{H}_{SSD} since \mathcal{H}_d mixes $c_k^\dagger |0\rangle$ and $c_{k \pm \delta n}^\dagger |0\rangle$. We now emphasize the important feature of SSD: g_{SSD} consists of the Fourier component of a single and shortest wave number δ as⁸

$$\begin{aligned} g_{\text{SSD}}(j) &= \cos \left[\frac{2\pi}{L} \left(j - \frac{1}{2} \right) \right] = \hat{g}_1 e^{i\delta j} + \hat{g}_{-1} e^{-i\delta j}, \\ \hat{g}_1 &= \hat{g}_{-1}^* = \frac{1}{2} e^{-i\frac{\delta}{2}}. \end{aligned} \quad (16)$$

Namely, the mixing via \mathcal{H}_d takes place only between the “nearest-neighbor” wave numbers in the discretized reciprocal space. Therefore, once we *fine tune the value of* chemical potential μ so as to set $\epsilon(k_g + \delta/2) = 0$, we could disconnect the states above and below this zero energy level [see Eq. (15) and Fig. 3(a)]. Due to Fermi degeneracy, \mathcal{H}_d cannot excite the particles except the one closest to the Fermi level, and since \mathcal{H}_d at that Fermi level is set to zero, one straightforwardly finds $\mathcal{H}_d |\Psi_{\text{PBC}}\rangle = 0$, which means that $|\Psi_{\text{PBC}}\rangle$ is now an eigenstate of \mathcal{H}_{SSD} .⁹

The coincidence between the PBC wave function and the SSD wave function for a fine-tuned chemical potential is further confirmed analytically in Refs. 10 and 11, and demonstrated numerically in Ref. 12 for the interacting system as well. This is the reason why the SSD is regarded as a smooth boundary condition that could suppress the boundary effect¹ discussed in the Introduction, and could recover the translational symmetry: it was the original idea presented by Nishino and collaborators who introduced SSD as well as other types of deformation to quantum lattice models.^{6,13}

However, aside from the boundary effect, the finite size effect still remains in the above fine-tuned SSD wave function. For example, the available values of the particle density $\langle n_i \rangle =$

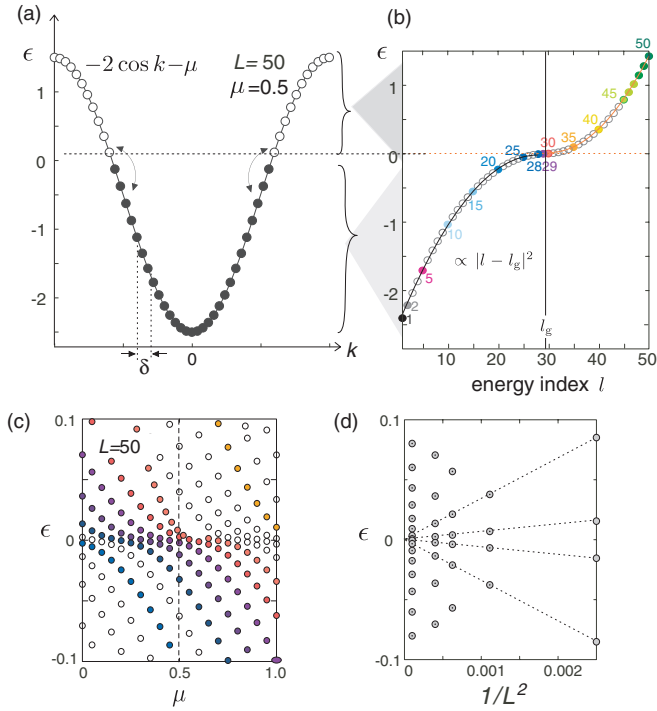


FIG. 3. (Color online) (a) Energy levels $\epsilon(k) = -2 \cos k - \mu$, with $k = \delta n$ for $L = 50$ and $\mu = 0.5$. (b) One-particle eigenenergies of \mathcal{H}_{SSD} for $L = 50$ and $\mu = 0.5$. The indices follow an ascending order from the lowest to the highest levels. (c) μ dependence of eigenenergies of \mathcal{H}_{SSD} at $L = 50$, and (d) $1/L^2$ dependence of eigenenergies at $\mu = 0$.

N_g/L are always a discretized rational number as in finite- L PBC. Also, Ref. 6 points out that the ground-state energy of SSD obeys L^{-2} , which is a typical size effect of PBC.

C. Mechanism of grand canonical setup

We now develop this formulation further, and finally show that the above idea of *getting the translationally symmetric PBC wave function by the fine tuning of μ in SSD is not the upper limit of availability* the deformation holds. Let us proceed by not confining μ to the “optimal value” for a given integer value of N_g , but instead *trying to get some optimal particle density for a given μ* .

We first simply diagonalize Eq. (9), and by filling the one-particle eigenstates from the lowest energy up to the zero energy level, we obtain the wave function $|\Phi_\mu\rangle = \prod_{\epsilon_l \leq 0} (\sum_{j=1}^N \varphi_l^*(j) c_j^\dagger) |0\rangle$. The total particle number is given as $N_\mu = \sum_{\epsilon_l \leq 0} \sum_{j=1}^N |\varphi_l(j)|^2$. This N_μ is nothing but the value that gave the lowest total energy (thermodynamic potential) in Fig. 2(d) in the grand canonical analysis. Indeed, if we increase or decrease the given particle number as $N_g = N_\mu \pm 1$, the energy increases because the positive/negative one-particle state is added to/removed from $|\Phi_\mu\rangle$. From now on, we consider this N_μ -particle state.

The lowest elementary excitation of $|\Phi_\mu\rangle$ is to add one-particle/hole as $\sum_j \varphi_{N_\mu \pm 1}^*(j) c_j^\dagger |\Phi_\mu\rangle$. Figure 3(b) shows the eigenenergy levels ϵ_l ($l = 1 \sim L$, from bottom to top). One finds that the low energy excitation levels concentrate at $\epsilon \sim 0$,

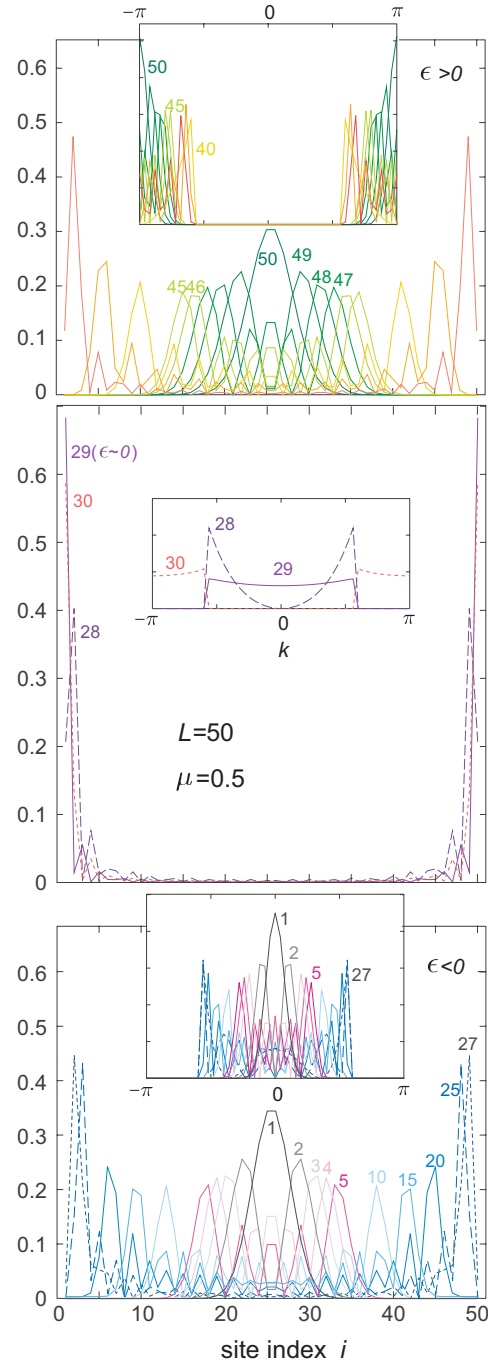


FIG. 4. (Color online) Profiles of eigenstates of \mathcal{H}_{SSD} $|\varphi_l(i)|^2$, at $L = 50$ at $\mu = 0.5$. The state indices $l = 1 \sim 50$ follow an ascending order from bottom to top of the energy, corresponding to Fig. 3(b). The edge states near zero energy level are $l = 28 \sim 30$, where $\epsilon_l \leq 0$ for $l \leq 29$.

in sharp contrast to the almost equally spaced sparse and discrete cosine energy levels of Eq. (12) with PBC [Fig. 3(a)]. With increasing system size, these concentrated states rapidly approach zero energy in proportion to $1/L^2$ as shown in Fig. 3(d).¹⁴

The spatial distribution of the one-particle eigenwave functions $|\varphi_l(j)|^2$ is plotted in Fig. 4. They form wave packets centered at different locations in real space. Here,

remind that due to the mixing term (\mathcal{H}_d), the eigenwave function takes the form of the superposition of the plane waves $\varphi_l(j) = \sum_k e^{ikj} \psi_l(k)$. (Wave packet is by definition a set of plane waves over a certain k region.) As the energy of the packet increases from the bottom of the energy band toward zero energy, the two peaks shift left and right, and at $\epsilon \sim 0$ the packets become the localized edge states.

How the edge states are constructed is understood by examining the eigenequation $\hat{H}_{\text{SSD}} \hat{\psi}_l = \epsilon_l \hat{\psi}_l$, where \hat{H}_{SSD} is the L -dimensional tridiagonal matrix with the off-diagonal $-\hat{g}_l \epsilon(k + \delta/2)$ and diagonal element $\epsilon(k)$, as given in Eq. (15), and $\hat{\psi}_l$ is a vector consisting of the wave function $\psi_l(k)$ ($k = \delta n$, $n = 1 \sim L$). By explicitly writing this eigenequation as

$$-\frac{1}{2} e^{i\frac{\delta}{2}\epsilon} \left(k - \frac{\delta}{2} \right) \psi_l(k - \delta) - \frac{1}{2} e^{-i\frac{\delta}{2}\epsilon} \left(k + \frac{\delta}{2} \right) \psi_l(k + \delta) = [\epsilon_l - \epsilon(k)] \psi_l(k), \quad (17)$$

one finds that, for small enough δ , at which $\epsilon(k - \delta/2) + \epsilon(k + \delta/2) \sim 2\epsilon(k)$ holds, the eigenvector of $\epsilon_l \sim 0$ should have a nearly k independent $\psi(k)$ over a certain range of k . Actually, the k profile of the edge states (see the inset of the middle panel of Fig. 4 with $l = 29$ and 30) consists of such uniform $|\psi_l(k)|^2$ at either $|k| \lesssim k_0$ or $|k| \gtrsim k_0$ [with $\epsilon(k_0) \sim 0$]. Then, its Fourier component $\varphi_l(j) = \sum_k e^{ikj} \psi_l(k)$ should indeed be a well-localized edge state, reminding that the delta function is the equally weighted superposition of plane waves.

The concentration of “edge states” near the zero energy level enables the continuous tuning of electron numbers away from the edges. This is because adding or removing few particles from the optimal value N_μ influences only the particle density near the system edges. Therefore, the center site of the system keeps the optimal value $\langle n_{L/2} \rangle \sim n_e$ we derived by the grand canonical analysis in Sec. II.

D. Accuracy

We finally evaluate the accuracy of $n_e \sim \langle n_{L/2} \rangle$. In the noninteracting fermionic system, the fitting of Eq. (11) gives the value of n_e that almost coincides with $\langle n_{L/2} \rangle$ within 10^{-5} . Note, however, that when the interaction is turned on, there arises an oscillation in $\langle n_i \rangle$ even at the center, so that the fitting operation in Sec. II is required in general. For simplicity, we examine $\langle n_{L/2} \rangle$ instead of n_e in the rest of this section. Figure 5(a) shows $\langle n_{L/2} \rangle$ as functions of μ varied over the whole energy band. The error against the exact solution n_{exact} is given in the inset and in Fig. 5(b); a sawtooth structure is found, roughly in a period of $\sim 1/L$ of a bandwidth. The edges of the sawtooth correspond to the place where the higher-energy level descends and crosses the zero energy. At this point, the integer $n_e L$ is realized and the wave function coincides with those of PBC as discussed in Sec. III B. In fact, by extracting the edges of these sawtooths in Fig. 5(b) for several L , the $1/L^2$ dependence is found [see the inset of Fig. 5(c)], and this gives the upper bound of the error of the present evaluation. Figure 5(c) shows the edge values of the sawtooth multiplied by L^2 over the whole range of μ . In the usual PBC analysis, the error is as large as *bandwidth*/ L , namely, ~ 0.1 for $L = 20$ and ~ 0.04 for $L = 50$ as indicated in Fig. 5(a) as height of the staircases. By contrast, our analysis keeps the error smaller

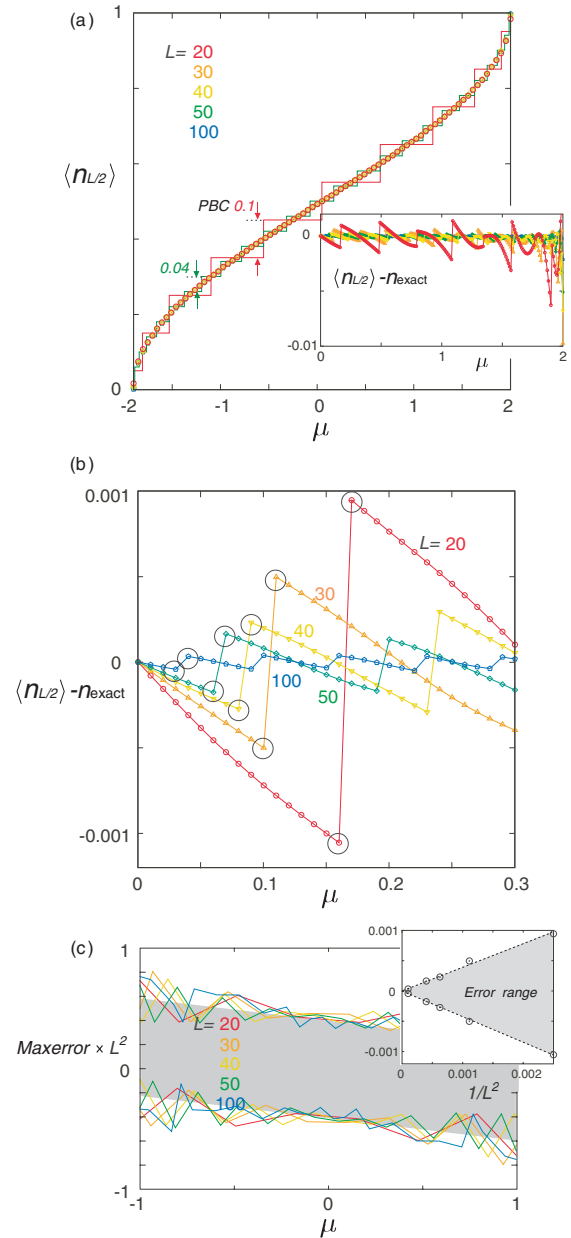


FIG. 5. (Color online) (a) Electron number at the center of the system $\langle n_{L/2} \rangle = \sum_{\epsilon_l \leq 0} |\varphi_l(L/2)|^2$, for $L = 20 \sim 100$. (b) Magnified error $\langle n_{L/2} \rangle - n_{\text{exact}}$, as part of the inset of (a). Their local maximum/minimum indicated as circles is plotted against $1/L^2$ in the inset of panel (c). (c) The local maximum/minimum of error multiplied by L^2 for $L = 20 \sim 100$.

than two orders of magnitude from those of PBC, typically as small as 10^{-4} .

IV. REAL SPACE RENORMALIZATION AND ENERGY SCALING

A. Wilson's NRG

The above-mentioned typical error, which is suppressed to several orders of magnitude from the typical finite size effect, indicates that the eigenstates have the scale-free character. To understand this, we refer to the Wilson's numerical

renormalization group (NRG),⁴ which is recently reexamined by Okunishi and Nishino as one of the most successful methods to afford the scale-free property of the low-energy excitations.¹⁵ The NRG starts from the derivation of the Hamiltonian by the so-called “logarithmic discretization” in reciprocal space, namely, by redefining the n th basis within $\Lambda^{-n-1} < |k| < \Lambda^{-n}$ in the original single-impurity Kondo Hamiltonian. The effective Hamiltonian is reduced to the following virtual 1D chain in k space with a modulated hopping term

$$\mathcal{H}_K^N = \sum_{n=1}^N \Lambda^{-n/2} (f_{n-1}^\dagger f_n + \text{H.c.}) - \tilde{J} f_0^\dagger \sigma f_0 \tau. \quad (18)$$

The first term corresponds to the kinetic energy of the conduction electrons and the last term indicates the scattering of the electrons by the single impurity placed at $n = 0$, with the coupling constant $\tilde{J} = 4J/(1 + \Lambda^{-1})$. Here, f_n^\dagger/f_n is the creation/annihilation operator of electrons on a lowest-energy basis state spanned in the n th discretized range $\Lambda^{-n-1} < |k| < \Lambda^{-n}$, which is described in real space as a rather localized Wannier-type orbital. The hopping integral $\Lambda^{-n} = e^{-n \ln \Lambda}$ rapidly decreases from zeroth to N th basis in k space, thus the characteristic length scale is given as $(\ln \Lambda)^{-1}$. This nonuniformity yields the energy spectrum which is dense at low energy. The renormalization is proceeded by adding an extra site at the opposite end from the impurity one by one, and at the same time, by multiplying $\Lambda^{1/2}$ to \mathcal{H}_K to keep the lowest energy to the order of unity as

$$\mathcal{H}_K^{N+1} = \Lambda^{1/2} \mathcal{H}_K^N + f_N^\dagger f_{N+1} + \text{H.c.} \quad (19)$$

The Hamiltonian finally reaches its fixed point $\tilde{J} \sim \infty$ (in the scale of Λ^{-N}) at a certain N depending on the value of Λ . This treatment succeeded in effectively taking in the correlation from short range to the longer range until the correlation of that length scale becomes irrelevant.

Okunishi and Nishino applied the idea of NRG to the non-interacting particle systems by adopting the idea of modulated hopping in the first term of Eq. (18) to a *real space* lattice Hamiltonian [to be precise, replacing n in Eq. (18) by a real space lattice index $j = 1 \sim L$, and taking Λ^n as a hopping], whose l th eigenvalue distributes logarithmically, $\epsilon_l \propto \pm e^{c|l-l_g|}$ (c : constant), as in Wilson’s case, where ϵ_{l_g} corresponds to the Fermi level.¹⁵ They found that the eigenstates $\phi_l(j)$ ($j = 1 \sim L$) form wave packets in real space, which follow the scale-free relation in their eigenvalue equation

$$\begin{aligned} \phi_l(j-1)\Lambda^{(j-1)/2} + \phi_l(j+1)\Lambda^{(j+1)/2} \\ = E_l \Lambda^{-(j-\frac{1}{2})} \phi_l(j) \Lambda^{j/2}. \end{aligned} \quad (20)$$

This means that by sliding the wave function by m -lattice spacing $j \rightarrow j+m$, the eigenenergy is scaled to $E_l \rightarrow E_l/\Lambda^m$. Thus, once we find a certain $\phi_l(j)$, the set of eigenstates and eigenenergies is obtained by the translation operation.

B. Deforming via NRG function

The main success of Wilson’s NRG was to extract the states of wide energy scales which contribute to the scattering at $n \sim 0$ near the Fermi level. In the present systems, we need a

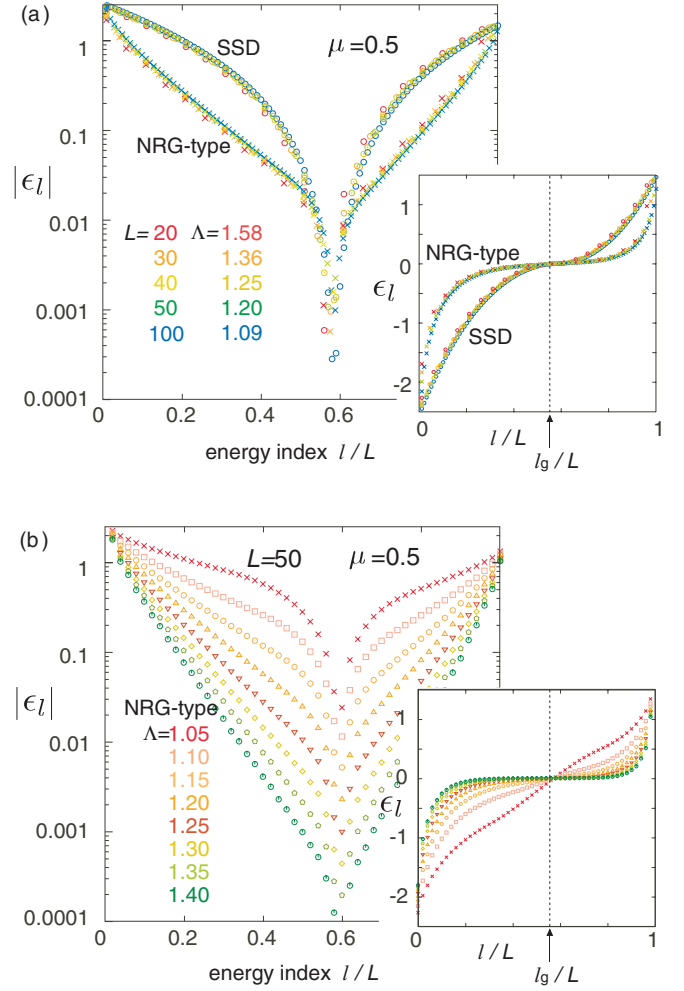


FIG. 6. (Color online) (a) One-particle eigenenergy ϵ_l of the deformed tight-binding Hamiltonian (9) using the NRG-type [Eq. (21)] function with $\Lambda = 10^{4/L}$ and SSD [Eq. (3)] function at $\mu = 0.5$. The horizontal axis scales the index of the level l by L . (b) The eigenenergy ϵ_l , under the variation of Λ , at $L = 50$ and $\mu = 0.5$. The insets of (a) and (b) show the same results on a linear scale.

bulk property *at the center of the system*. Therefore, it is natural to apply the NRG type of modulation to our formulation as

$$f_{\text{NRG}}(j) = \Lambda^{-|j-(L+1)/2|} \quad (21)$$

and proceed our analysis following Sec. II. This corresponds to shifting the $n = 0$ point in k space in Wilson’s NRG to $L + 1/2$ (center of the system) point in real space in our system, and forcing the energy to scale down to nearly zero at edges of the fixed L , instead of increasing L by the renormalization. Figure 6(a) shows the comparison of one-particle eigenenergies ϵ_l ($l = 1, \dots, L$), obtained by deforming the noninteracting Hamiltonian (8) in two ways using Eqs. (21) and (3). Here, for f_{NRG} we use $\Lambda = 10^{4/L}$ in order to suppress f_{NRG} to the same orders of magnitude at the edge sites for different L ’s. In both types of deformation, the eigenenergies are scaled to the single functional form, with a large density near $\epsilon_l \sim 0$. The Λ dependence of the energy level is also examined in Fig. 6(b) at a fixed $L = 50$. One sees that ϵ_l indeed follows the powers of Λ , and that one needs to take sufficiently large Λ to make the energies accumulated near the zero energy.

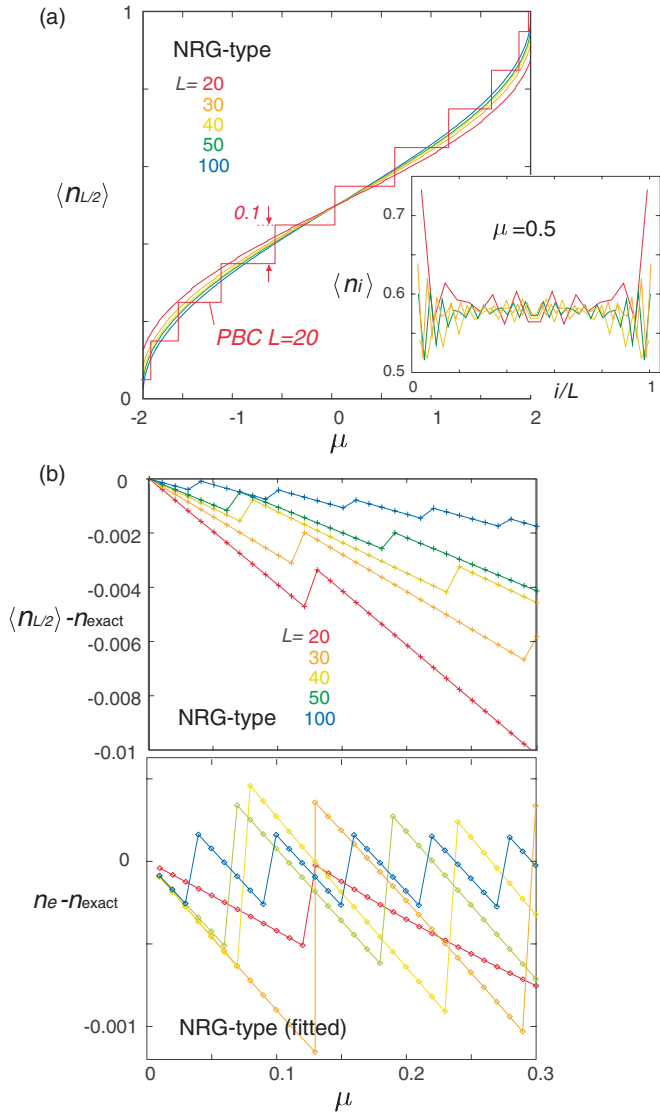


FIG. 7. (Color online) Results of the deformed Hamiltonian using the NRG-type [Eq. (21)] function with $\Lambda = 10^{4/L}$. (a) Electron number at the center of the system $\langle n_{L/2} \rangle$ for $L = 20 \sim 100$. The inset shows the spatial profile of the electron density $\langle n_i \rangle$ at $\mu = 0.5$ and $L = 20, 30, 40$. (b) Errors of the raw electron number in (a) $\langle n_{L/2} \rangle - n_{\text{exact}}$ (upper panel) and those of the fitted result $n_e - n_{\text{exact}}$, using Eq. (11) excluding $r \leq 2$ from the fitting range.

The above results seemingly suggest that the SSD function could be replaced by the NRG function, so that the intrinsic properties of our formulation had already been covered by NRG. This is, however, not necessarily the case. Figure 7 shows the results of the grand canonical analysis of the 1D free-fermionic system with f_{NRG} , to be compared with those of the SSD in Fig. 5. As shown in the inset of Fig. 7(a), the oscillation of $\langle n_i \rangle$ is very large [compare with Fig. 5(a)]. Indeed, the center site $\langle n_{L/2} \rangle$ no longer gives accurate enough results in NRG. The error amounts to one order of magnitude larger than the SSD case [see the upper panel of Fig. 7(b)]. In order to exclude the effect of oscillation, we carefully fitted $O(r)$ of the NRG results following Eq. (11) by excluding $r \leq 2$ (center site) from the fitting range. This is because the

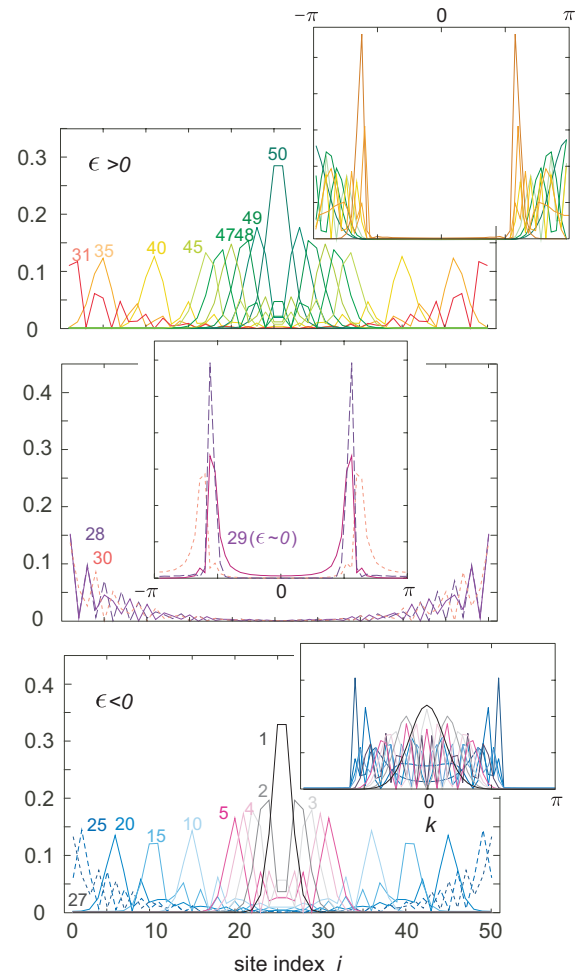


FIG. 8. (Color online) Profile of the eigenstates $|\varphi_l(i)|^2$ of the deformed Hamiltonian of tight-binding fermions by the NRG type of function [Eq. (21)] with $\Lambda = 10^{4/L}$, $L = 50$, and $\mu = 0.5$, to be compared with those of SSD in Fig. 4. The state indices follow an ascending order from the bottom to the top of the energy $l = 1 \sim 50$. The insets show the corresponding Fourier component in the momentum space.

oscillation prominent even at the center gives a large error if we include $r \leq 2$. The results given in the lower panel of Fig. 7(a) are suppressed to reasonable values. Still, the SSD function gives better results.

Figure 8 shows the profile of the wave function of the NRG deformation $|\varphi_l(i)|^2$ to be compared with Fig. 4 (SSD), on a same vertical scale. Similar to the report by Okunishi and Nishino, the eigenstates of \mathcal{H}_{NRG} form wave packets in a quite similar manner to those of \mathcal{H}_{SSD} . However, there is a distinct difference. As shown in the middle panel, the states near the zero energy ($l = 28, 29, 30$) are no longer real “edge states,” but are distributing over several sites. In fact, the k profile of these states shown in the inset have a sharp peak, which means that the corresponding wave packet is not well localized (see the flat k profile of the SSD case). Since our grand canonical mechanism is supported by the formation of good edge states, the NRG deformation turned out to be less suitable.

C. Scale-free properties of SSD

Despite the differences discussed above, the NRG still shares a scale-free concept with the SSD deformation. Let the deformed Hamiltonian (2) be spanned by the real space basis $c_j^\dagger|0\rangle$ ($j = 1 \sim L$). The eigenequation is given as $\hat{H}_{\text{deform}}\hat{\phi}_l = \epsilon_l\hat{\phi}_l$, with $\hat{\phi}_l$ the vector whose j th element is $\phi_l(j)$. Since \hat{H}_{deform} has the tridiagonal form, the eigenequation is written along its j th row ($2 \leq j \leq L/2 - 1$) as

$$\begin{aligned} -f\left(j - \frac{1}{2}\right)\phi_l(j-1) - f\left(j + \frac{1}{2}\right)\phi_l(j+1) \\ = [\epsilon_l + \mu f(j)]\phi_l(j). \end{aligned} \quad (22)$$

Now, it is natural to expect

$$r_j \equiv \frac{f(j+1)}{f(j)} \sim \frac{f(j + \frac{1}{2})}{f(j - \frac{1}{2})} \quad (23)$$

for a gradually varying function and for large enough L . Then, after shifting the index as $j \rightarrow j+1$, all the terms of Eq. (22) are roughly scaled by r_j times only if we replace the energy as $\epsilon_l \rightarrow r_j\epsilon_l$. Therefore, if $\epsilon_{l+1}/\epsilon_l \sim r_j$ holds, the corresponding eigenfunctions show a scale-free property: sliding the wave function $\phi_l(j)$ by one lattice spacing will give us $\phi_{l+1}(j+1)$. Indeed, in the case of SSD, the wave function follows the relation

$$|\phi_{l-1}(j-1)|^2 + |\phi_{l+1}(j+1)|^2 \sim 2|\phi_l(j)|^2 \quad (24)$$

in analogy to Eq. (20). This can be viewed in Fig. 4 noticing that the l th wave packet has a peak at $j \sim (L+1)/2 \pm (l-1/2)$. The coincidence of the left- and right-hand sides of Eq. (24) is larger than 90% except at the very vicinity of the edges.

In the case of f_{NRG} , $r_j = \Lambda$ is a constant, whereas for f_{SSD} , r_j is a gradually decreasing function. Figure 9(a) shows $\epsilon_{l+1}/\epsilon_l$ as a function of $(l-l_g)/L$. In both cases, $\epsilon_{l+1}/\epsilon_l$ is in good agreement with r_j . Namely, both SSD and NRG have the scale-free property via $\epsilon_l \propto f_{\text{NRG}}$ and f_{SSD} , respectively.

However, in the vicinity of the band edge ($l-l_g \sim L/2$), $\epsilon_{l+1}/\epsilon_l$ falls off r_j and becomes slightly larger than 1. Notice that the energy scaling occurs in the opposite direction in real space at $j \leq L/2$ and $j > L/2$, and near the system center, the two scalings mix, which would be the reason for such deviation. This could be viewed more clearly in Fig. 9(b); ϵ_l follows overall the deformation function, but near the band edge $(l-l_g)/L \sim 0.5$, it increases toward $\epsilon_l \rightarrow 2$ instead of unity ($f \rightarrow 1$). In the case of SSD, $f_{\text{SSD}}(j) \propto j^2$ holds at small j , and the deformed energy level continues to follow this curve as $\epsilon_l \propto (l-l_g)^2$ toward the band edge. The deviation from the scaling function is thus preferable to reproduce the energy near the band edge. Otherwise, the scaling will work as an advantage only near zero energy, and our grand canonical analysis would become unsuccessful.

Now, let us project $\langle n_{L/2} \rangle$ to each energy level by taking the right-hand side of

$$\langle n_{L/2} \rangle = \sum_{\epsilon_l \leq 0} |\phi_l(L/2)|^2. \quad (25)$$

The inset of Fig. 9(c) shows the distribution of $|\phi_l(L/2)|^2 \times L$ as a function of ϵ_l for different L in the SSD deformation. One finds that the profile exactly follows the universal curve.

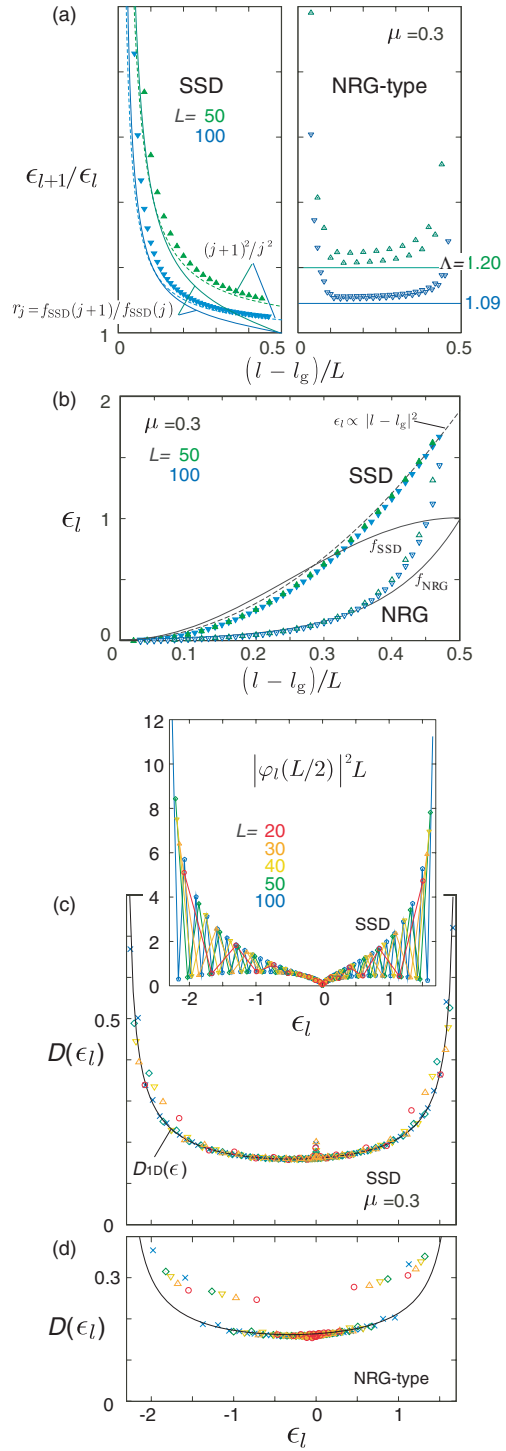


FIG. 9. (Color online) Comparison of quantities of the tight-binding fermionic Hamiltonian deformed by the SSD and NRG functions at $\mu = 0.3$. (a) Ratio $\epsilon_{l+1}/\epsilon_l$ compared with $r_j = f(j+1)/f(j)$ in solid line as a function of j/L [$\leftrightarrow (l-l_g)/L$] for $L = 50$ and 100 . The left and right edges of the horizontal axis are the chemical potential level $\epsilon_{l_g} = 0$ and the top of the band $(l-l_g)/L = 0.5$, respectively. (b) Energy levels ϵ_l compared with f_{SSD} and f_{NRG} , as well as $c|l-l_g|^2$. (c) Inset: Local electron number projected to each energy level, scaled by the system size as $|\phi_l(L/2)|^2 L$ for $L = 20 \sim 100$. (c), (d) The density of states obtained from Eq. (26) and the inset data (SSD). The exact density of states of the 1D free tight-binding particles [$D_{1D}(\epsilon)$] is shown together in the solid line.

Anticipating from the way of distribution of energy, we calculate

$$\begin{aligned} D(\epsilon) &= \frac{d \sum_{\epsilon_l \leq \epsilon} |\varphi_l(L/2)|^2}{d\epsilon} \\ &= \frac{|\varphi_l|^2 + (|\varphi_{l+1}|^2 + |\varphi_{l-1}|^2)/2}{\epsilon_{l+1} - \epsilon_{l-1}} \end{aligned} \quad (26)$$

by taking the difference differential for $\epsilon \sim \epsilon_l$, and smoothing out the even-odd oscillation and plot it in Fig. 9(c). We find that it coincides with the 1D density of states $D_{1D}(\epsilon) = \pi^{-1} d \arccos(-\epsilon/2)/d\epsilon$. This coincidence is kept irrespective of the value of μ or of L . The SSD deformation forces the energy levels to concentrate near zero but still *keeping enough numbers of states at the band edges* in a way to thoroughly reproduce the bulk density of states. This energy scaling essentially overcomes the fundamental problem of discreteness in energy levels, which were inevitably reflected in the physical quantities in a general treatment.

We also calculate $D(\epsilon)$ for the NRG type of deformation and plot it in Fig. 9(d) for comparison. Again, the data at $-1 \lesssim \epsilon \lesssim 1$ are in good agreement with $D_{1D}(\epsilon)$, but outside this region it suddenly falls off the 1D curve, and the van Hove singularity at the band edge is no longer reproduced. The eigenstates near this band edge correspond to the wave packet localized at the center of the system. Therefore, the failure in reproducing the largest energy scale disproportionately affects the bulk eigenstate near the center of the system. This should be responsible for the large oscillation induced in the NRG type of deformation in Fig. 7(a), which leads to the large error. The SSD deformation thus turns out to be the optimal function to reproduce the energy structure over the whole energy scale, while concentrating the levels near the chemical potential, still not sacrificing those far off that level.

V. QUANTUM MANY-BODY SYSTEMS

We have shown in the noninteracting systems that the SSD deformation worked *to generate the edge states which concentrate near the zero energy*. This enables us to easily tune the particle density to the optimal value at the center of the system since, at the center, the edge states near zero energy have the amplitude of less than 10^{-4} . The same thing happens even if we turn on the interaction.

The demonstration is given on a series of $S = \frac{1}{2}$ Heisenberg antiferromagnet for representative lattices, the 1D chain, square lattice, and a regular triangular lattice. The Hamiltonian without deformation is given as

$$\mathcal{H} = \sum_{\langle i,j \rangle} S_i \cdot S_j - h \sum_{i=1}^N S_i^z, \quad (27)$$

where S_i and S_i^z are the $S = \frac{1}{2}$ spin operator and its z component. The interaction is taken over all nearest-neighbor sites $\langle i,j \rangle$. The results throughout this section are obtained by the DMRG, which is considered to be one of the most successful numerical solvers in low dimension¹⁶ and is applicable even to the frustrated lattices. For 1D, we take the maximum number of states kept per block to be $m = 300$, which suppresses the truncation error to be less than the order of $10^{-7} \sim 10^{-8}$. In 2D, we take maximally $m = 5000$, with

the typical truncation error of 10^{-6} . However, we find that the truncation errors could be kept more roughly. The accuracy of the grand canonical analysis almost does not depend on the truncation error, as far as it is kept less than the order of 10^{-5} .

A. 1D system

We first show the analysis given for the 1D chain to be compared with those of the noninteracting fermions in Sec. II. Figures 10(a) and 10(b) are the spatial distribution of $\langle S_i^z \rangle$ and its average

$$O(r) = \frac{1}{2r} \sum_{i=-r}^{r-1} \langle S_{i+\frac{1}{2}}^z \rangle, \quad (28)$$

which is the quantum spin version of Eq. (10). They show the results qualitatively equivalent to Figs. 2(a) and 2(b). The difference from the noninteracting case lies in the relatively enhanced oscillations with a short-range period, even at the center of the system. Note that this is not the Friedel oscillation since the energy of the boundary is almost suppressed to measure zero. This oscillation rather comes simply from the breaking of the translational symmetry. If the interaction is strong enough, the short-range correlation develops, which tries to make the neighboring spins antiparallel. Since we do not have any external effect from the boundary to suppress such oscillation, they behave freely just as in the bulk limit, and the edge of the oscillation is absorbed smoothly by the free boundary. The magnetization curve obtained by the fitting $O(r) = M/L + cr^2$ is given in Fig. 2(c), which is in good agreement with the exact solution just as in the noninteracting system with the same order of error. The evaluated error for several different M_g/L is shown as a function of $h \sim 1$ in Fig. 10(d). In this case, if we take $M_g = 6-7$ for $L = 50$ ($\Delta M_g/L \lesssim 0.05$ as discussed in Sec. II), one can suppress the error to be $\sim O(10^{-4})$ in a range of $\Delta h \sim 0.1$. For more information, see Ref. 3.

B. 2D systems

The case of 2D also turned out to be successful. Figure 11(a) shows the magnetization curve obtained by the Cartesian SSD with $N = 8 \times 8 = 64$ and by the polar SSD with $N = 80$ shown in the inset, where we filled the circle with sites in order to lessen the effect from the boundaries. The results of the polar SSD are particularly in good agreement with the results obtained by the second-order spin-wave theory (SWT).¹⁷⁻¹⁹ On the other hand, the Cartesian ones deviate slightly ($\sim 10^{-2}$) upward near the saturation field. Figure 11(b) shows the spatial distribution of $\langle S_i^z \rangle$ along the cuts of the square lattice with polar deformation, which is indicated as bold arrows in the inset of Fig. 11(a). A similar profile with those of the noninteracting system (see Appendix A and Fig. 17 for details) is found. Here, $\langle S_i^z \rangle$ is almost flat over about 10 sites near the center for $h \lesssim 3$. However, it starts to show a curve near the saturation field. This kind of curve is present also in 1D, but its artifact is smaller since the system length L is larger than one could take in 2D ($\sim 10 \sim 20$). This is mainly the reason why the accuracy of the results in 2D near the saturation field becomes as worse as to be visually detected

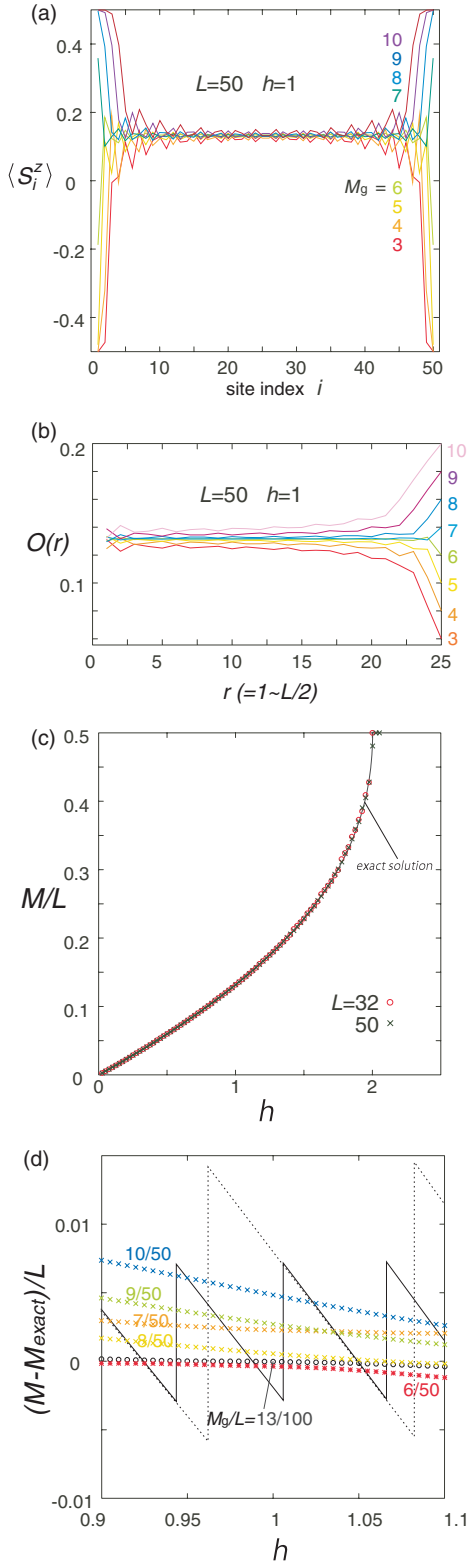


FIG. 10. (Color online) Analysis on the $S = \frac{1}{2}$ Heisenberg chain. (a) Expectation value of the local magnetization density $\langle S_i^z \rangle$ of the SSD Hamiltonian for various choices of M_g . (b) $O(r)$ in Eq. (28) as a function of r . (c) M/L obtained by fitting $O(r)$. The smooth solid line represents the exact solution. (d) Error $(M - M_{\text{exact}})/L$ as a function of $h \sim 1$ for several choices of M_g/L . Solid and broken lines represent those obtained by the standard OBC-DMRG with $L = 50$ and 100 , respectively.

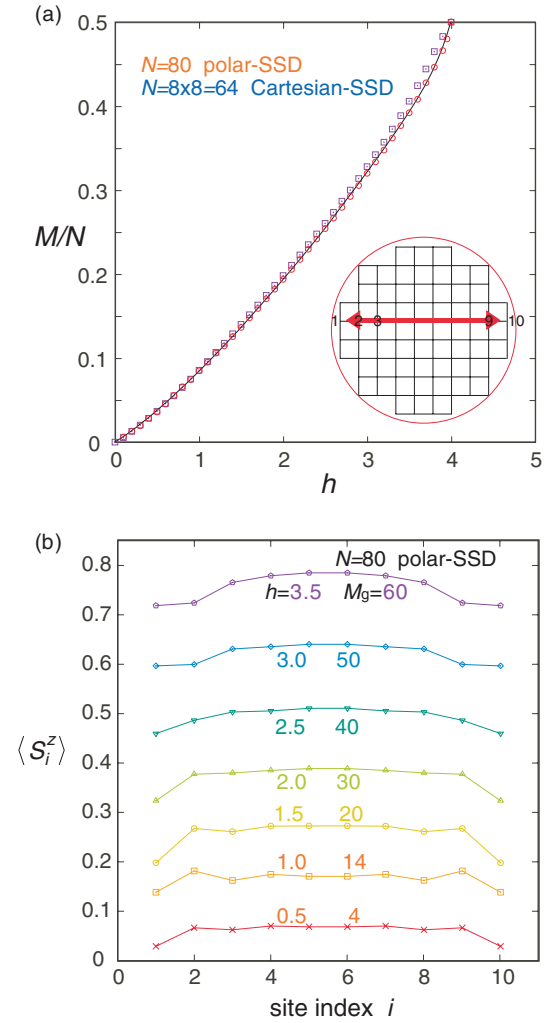


FIG. 11. (Color online) Grand canonical analysis on the $S = \frac{1}{2}$ Heisenberg model on a square lattice using the Cartesian SSD with $N = 8 \times 8 = 64$, and polar SSD with $N = 80$ shown in the inset. (a) Magnetization curve M/N as a function of magnetic field h . Solid line represents the result of the second-order spin-wave theory (Refs. 17–19). (b) Expectation value of the local magnetization density $\langle S_i^z \rangle$ in the case of polar SSD with $N = 80$ along the cut of the cluster shown in the inset.

in the M - h curve, in which case one needs careful treatment, e.g., try different deformations or tune M_g .

Next, we show the case of the triangular lattice. There are several results based on the exact diagonalization, indicating the existence of the $\frac{1}{3}$ plateau.^{20–22} Meanwhile, their shape remains a staircase due to the finite size effect. The SWT²³ is also less accurate compared to the case of the square lattice. Here, we compare our results with the coupled cluster method (CCM), which so far has succeeded in obtaining the smooth curve.²⁴ This CCM includes the multispin cluster correlations over m -site cluster, which is the approximation called the localized LSUB m . In the limit of $m \rightarrow \infty$, the CCM gives the exact result (while it is practically out of hand).

Figure 12(a) shows the M - h curve obtained by the present analysis on a hexagonal $N = 75$ cluster with polar SSD and on a three-leg cylinder with quasi-1D SSD and $N = 126$,

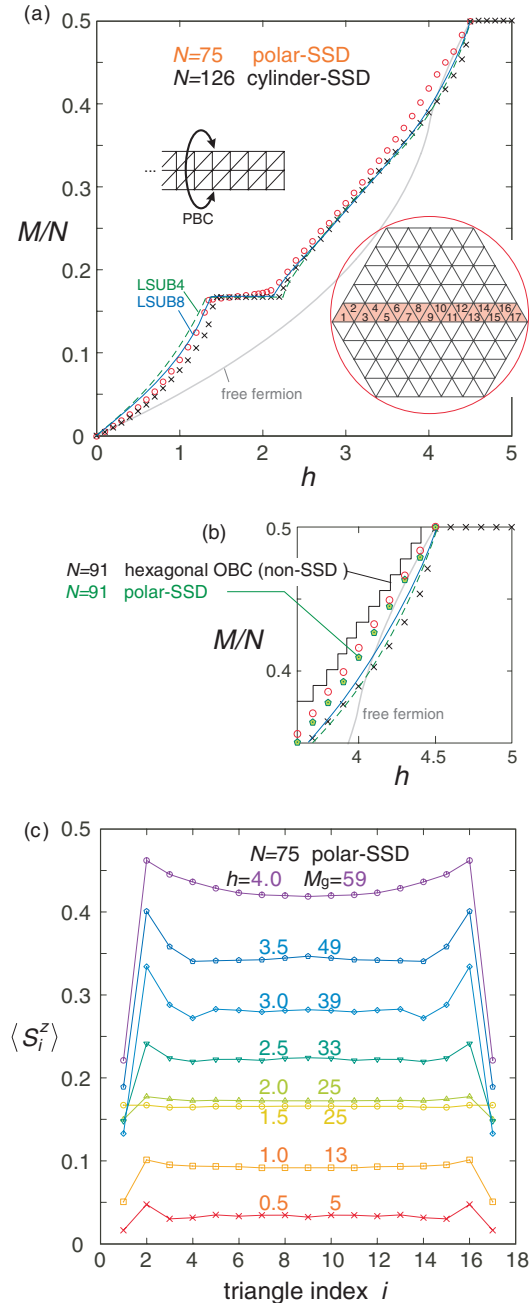


FIG. 12. (Color online) (a) Magnetization curve M/N as a function of magnetic field h on the long cylinder with quasi-1D SSD ($N = 126$) and on a hexagonal cluster with polar SSD ($N = 75$), shown in the inset. The broken and solid lines are the LSUB4 and LSUB8 results of the CCM from Ref. 24. The solid gray line is the bulk $\mu - \rho$ curve of the free fermion on a triangular lattice [the same as Fig. 18(a) in Appendix C]. (b) Magnified curve near the saturation field in (a), with additional results put together for $N = 91$ irregular hexagonal cluster [Fig. 1(e)] both with polar SSD and with open boundary (solid line). The cylinders SSD (the infinite-length limit) with steep curve slowly approaches the linear slope of the hexagonal polar SSD representing those of the true 2D bulk limit. We consider that the LSUB m including the m th correlations give comparable results with the m -circumference cylinder, in consistency with our results. However, the polar SSD has closer value to the bulk triangular lattice. (c) Expectation value of the local magnetic density $\langle S_i^z \rangle$, averaged within each triangular unit, is shown in the inset of (a).

which are shown in the inset. The long cylinder is often used in 2D DMRG to obtain accurate numerical results (for that size) comparable to those of 1D, which is also considered as convenient to carry out a systematic size scaling. Recently, however, Sandvik²⁵ pointed out a severe artifact of taking the aspect ratio of the cluster to be less than $\frac{1}{10}$, particularly when the order or correlation of a period longer than/incompatible with the circumference of the cylinder. Therefore, interpreting the results of the cylinder as those of the bulk needs care.

In the CCM-LSUB m approach, the triangular lattice is divided into three sublattices,²⁴ taking in the fluctuation of m th lattice spacing, thus effectively considering a rather narrow region comparable to those of a long cylinder with m circumference. In fact, as shown in Fig. 12(a), the LSUB m results agree very well with the results of our cylinder for all ranges of h . Here, note that our cylinder SSD represents only the result of the 1D infinite-length limit of that circumference. The M - h curve for the three-leg cylinder shows a steep increase near the saturation field, as is often the case with (quasi-)1D quantum systems. In general, the slope becomes less steep with increasing numbers of coupled chains, due to a suppression of the quantum fluctuations by antiferromagnetic interchain couplings.²⁶ With this in mind, we take a careful look at the magnified curves near the saturation shown in Fig. 12(b); the steepest curve is obtained for our three-leg cylinder, and right up this curve we find a series of LSUB m , which shifts upward with increasing m . On the other side, a series of polar SSD hexagonal clusters, which has an ideal aspect ratio, shows an almost linear curve near the saturation. Here, we find that the size effect ($N = 75$ and 91) is smaller than 10^{-2} in these worst cases near the saturation field, which is the advantage of our grand canonical analysis. For another reference, we plot the DMRG result on the same hexagonal cluster ($N = 75$) with usual open boundary (without SSD) as staircases by carefully checking that the open boundary does not impose any artifact on the result in this parameter range. We also confirmed that with increasing N , the staircase shifts rightward, approaching the polar SSD curve. Therefore, it is likely that the polar SSD with aspect ratio 1 represents the bulk curve.

To further confirm this, we plot the free-fermionic curve both in Figs. 12(a) and 12(b) (see also Fig. 18 and Appendix C), and find that they coincide well with the two linear curves by the polar SSD near the saturation field and near the zero field. It is known that the elementary particles representing these curves are $S = 1$ magnons (hard-core bosons), and the magnetic field serves as a chemical potential of the magnons. At $M/N \sim 0$ or 1 , the magnons ($S_z = 1$ and -1 , respectively) are dilute, so that they could be approximated by the dilute free fermions. Thus, we conclude that by varying the aspect ratio toward unity, the curve approaches very slowly from the steep ones and finally reaches the proper bulk curve, mimicking our hexagonal polar SSD one.

The effort to systematically analyze the effect of aspect ratio is given in the 2D DMRG study.²⁷ In fact, in the usual 2D DMRG with open ends (including those of cylinders), the results are more sensitive to the small change in the aspect ratio than in the present analysis. This is presumably because the shape or the period of the lattice directly influences the discrete values of k . In our case, the results are much more influenced by the shortest sidelength of the lattice than the aspect ratio

itself. Therefore, for a fixed N , the closer the aspect ratio is to unity, the more reliable the results become, since the shortest sidelength becomes longer. The details in the case of square lattice are given in Appendix D.

Again, it will be of help to have a look at the spatial profile of $\langle S_i^z \rangle$ in Fig. 12(c), which is obtained by taking an average in unit of a single triangle indicated in the inset of Fig. 12(a). This is because, in contrast to the case of a square lattice, there arises a strong oscillation of a threefold periodicity, which is possibly due to the strong correlation between spins arising from the frustration effect. The resultant profile is smooth enough to obtain the value mimicking its thermodynamic limit by our analysis. Similarly to the case of the square lattice, it is almost flat over about 10 triangular units near the center for $h \lesssim 3.5$ and it starts to show a smooth curve at $h \gtrsim 3.5$. Still, the profile converges to an adequate value near the center even at high field $h = 4$. We also mention that near the plateau or the saturation field, one needs to tune M_g to check whether there are no other solutions with lower energies, in order to confirm the reliability of the result.

Next, we evaluate the range of the plateau. Note that the accuracy of our analysis near the plateau (gapped state) is less guaranteed compared to those in the critical case (see Appendix A for details). From the data presented in Fig. 12(a), we find $1.35 \leq h \leq 2.10$ and $1.40 \leq h \leq 2.20$ for the polar hexagon and cylinder, respectively, within the error of 0.01. These values are in good agreement with LSUB8 $1.370 \leq h \leq 2.145$,²⁴ while the SWT result $1.248 \leq h \leq 2.145$ is rather overestimating the onset of the plateau.

So far, there are not so many relevant laboratory systems on this $S = \frac{1}{2}$ triangular lattice antiferromagnet: Cs_2CuCl_4 (Ref. 28) is a distorted triangle and Cs_2CuBr_4 ,^{29,30} whose magnetization curve is reported, is not a simple Heisenberg antiferromagnet but has a relevant Dzyaloshinsky-Moriya interaction. Recently, $\text{Ba}_3\text{CoSb}_2\text{O}_9$ ³¹ showed up as an ideal candidate, which reveals a comparable M - h curve to those of the previous studies, while the plateau is rather inclined possibly due to the anisotropy of the g factor and interactions in powder samples. Their experimental slope near the saturation field is almost linear in field, to be compared with our latest results.

VI. CONCLUSIONS

This paper showed that the grand canonical analysis could be successfully performed on the 1D and 2D interacting systems as well as on the trivial noninteracting cases. In usual quantum many-body calculations on lattice models, the conserved quantities, such as the total electron number and total S^z (N_g and M_g in this paper), are integers given by hand, and their conjugate fields, the magnetic field h , and the chemical potential μ are automatically determined. The electron or magnetization densities thus obtained are discrete rational numbers N_g/L or M_g/L for each lattice size L . On the contrary, in our analysis, we fix the external field h or μ by hand, and obtain the electron or magnetization density N_e/L ($\neq N_g/L$) or M/L ($\neq M_g/L$), which are the *continuous functions* for a given external field with the accuracy of $\sim 10^{-4}$. This became possible by systematically generating a well-localized edge state of measure zero energy, which serves as “particle bath.” The “bulk” state spreading at the

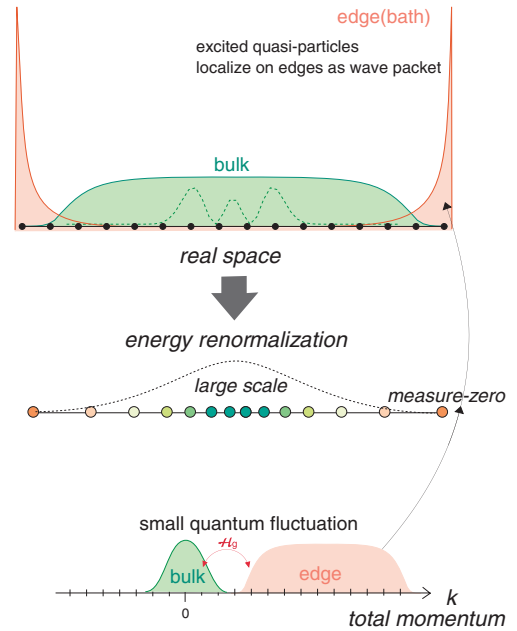


FIG. 13. (Color online) Sketch of the setup of the grand canonical analysis, relating the real space and momentum space description of the low-energy states.

center of the system is smoothly connected to the “bath” by the infinitesimally small quantum fluctuation.

As we discussed in Secs. III and IV, the key concept to understand this rather counterintuitive mechanism is the *wave packet* (see also the schematic description in Fig. 13); in usual quantum lattice systems, the wave number k is a good quantum number, and the eigenstates are basically described as *plane waves*. Contrarily, in the present system, *the eigenstates are the wave packets localized in real space*. As is well known, the wave packets are the superpositions of plane waves ranged at some $k_c - dk \leq k \leq k_c + dk$, and they become more localized for larger dk . To generate such wave packets in the present framework, we introduce the additional term to the Hamiltonian $\mathcal{H} \rightarrow \mathcal{H}_{\text{deform}} = \mathcal{H} - \mathcal{H}_d$. It smoothly scales down the energy unit of the Hamiltonian in real space from the maximum at the center to zero at open edges. In reciprocal space, \mathcal{H}_d mixes the k th and $(k + \delta n)$ th eigenstates of the original \mathcal{H} in an amplitude proportional to the their original eigenvalue. The wave packets are thus generated by the mixing of plane waves within finite dk . Particularly, the packets made out of dk over almost half the Brillouin zone are the localized edge states. Since the edges have the measure zero energy due to the deformation ($\mathcal{H}_{\text{deform}} \sim 0$ at the edges), they are concentrated at the chemical potential level. In this way, the wave packets have their own energy scale depending on which region they are localized in real space; The ones at the center have large energy and light mass, contributing to the bulk state. Those at the edges have heavy mass and can hardly move, serving as bath. The energy levels are thus redistributed in a way that the energies closer to zero have larger density, and to reproduce the shape of the density of states over the whole energy range. The wave-packet wave functions have a scale-free character, in the sense that those with different energy scales could be generated one by one by sliding them to the neighboring site.

The deformed Hamiltonian can be partially regarded as an analog of Wilson's numerical renormalization group (NRG) Hamiltonian, which has a spatially modulated hopping term. Indeed, the NRG Hamiltonian also generates a wave-packet eigenstate of a scale-free character.¹⁵ The NRG framework succeeded in keeping all different energy scales joining the physics by gradually scaling down the energy in increasing the system size L . The resultant energy unit varies from maximum at one edge to the minimum on the other end. Once L exceeds some critical value, the system reaches a fixed point and the eigenstates become scale free. On the other hand, in our setup, such "real space" renormalization was not actually carried out, but instead, we forced the energy scales to go down from maximum at the center to zero on the edges. However, this rather crude setup generates an energy structure comparable to that of NRG. This is the origin of a considerably small system-size dependence of the physical quantities we obtained.

As a deformation function, we mainly adopted the sine-square function (SSD), first introduced as a novel type of smooth boundary condition by Nishino and collaborators.⁶ In Sec. III, this function turned out to be the optimal function in the sense that it consists of *a single wave of the wavelength exactly covering the whole system*. Since the mixing between k and $(k + \delta n)$ states takes place for δn with a finite Fourier component of the deformation function, the shortest and single wave number ($n = 1$) of the SSD works to generate both the well-localized edge states and the moderate wave packets at the center which could smooth out the oscillation of the physical quantities. We have tested several functions, such as NRG type (Sec. IV), Fermi-distribution function, or power functions (Appendix B), but they all turned out to be less efficient. Particularly, the generation of a good (well-localized) edge state is rather unsuccessful compared to SSD.

In this way, our grand canonical analysis using the SSD optimally realizes the bulk eigenstate basis at the center of the small finite cluster. The bulk state spanned by the wave packet is constructed by forcing the energy scaling similar to that of NRG by hand. A series of quasiparticle edge states are generated as lowest-energy excitations, and serve as buffer to tune the particle density toward its bulk limit. We applied this analysis from solvable free-fermionic systems in 1D (Secs. II and III) and 2D (Appendix C), to the interacting spin systems (Sec. V) and to the strongly interacting electron systems (Appendix B). There, we found that the present analysis gives quantitatively comparable accuracy, regardless of whether the interactions are present or not. (For more information on the results of the interacting system, see Ref. 3.) The advantages of the present framework are the applicability (easy coding) and the handiness of the analysis with no extra tunable parameters that dominate the accuracy (e.g., in DMRG the tunable parameter is a truncation error or the number of states kept per block). One could even reduce the numerical cost by abbreviating the finite size scaling analysis (while instead one needs to calculate more data points to have a smooth curve). Thus, our method, with its background thus clarified, shall accelerate the clarification of many unknown phenomena in low-dimensional quantum many-body systems, which is one of the most celebrated research areas in the past several decades in condensed matter physics.

ACKNOWLEDGMENTS

We acknowledge I. Maruyama and H. Katsura for discussions, and H. Nakano, T. Tonegawa, and A. Shimizu for comments. This work is partially supported by a Grant-in-Aid for Scientific Research (No. 20102008) from the Ministry of Education, Science, Sports and Culture of Japan.

APPENDIX A: GAPPED SYSTEMS

This paper dealt with the case where the chemical potential lies within the energy bands. However, once it is within the gap, the applicability of SSD is no longer valid.⁶ In Sec. V, it turned out that the plateau (gapped region) in the triangular lattice was detected in relatively good agreement with the results of other methods. Meanwhile, one shall find that the plateau by the polar SSD [see Fig. 12(a)] has a finite gradient. Such gradient indeed appears in the general cases we discuss in this Appendix. Here, we systematically analyze the general gapped system.

As a representative 1D gapped system, we introduce the t_1 - t_2 model, a noninteracting system with alternating transfer integrals along the chain

$$\mathcal{H}_{t_1 t_2} = \sum_{j=1} (t_1 c_{2j-1}^\dagger c_{2j} + t_2 c_{2j}^\dagger c_{2j+1} + \text{H.c.}), \quad (\text{A1})$$

whose energy band

$$\epsilon_{\pm}(k) = \pm \sqrt{(t_1 + t_2) \cos^2 k + (t_1 - t_2) \sin^2 k}$$

has a gap $\Delta = 2|t_1 - t_2|$. When we deform this Hamiltonian, one easily finds that the term \mathcal{H}_d mixes the states of upper and lower bands. Resultantly, there arises an in-gap state, whose artifact on the grand canonical analysis is nontrivial. Figure 14(a) shows the electron density at the center of the system when μ varies from the center of the gap ($\mu = 0$) toward above the gap. At $L = 20$, the deviation from 0.5 within the gap is very large, which is rapidly suppressed with increasing L , particularly when the gap is large (right panel). We plotted the error at the point where the gap closes, namely, $\mu = \Delta/2 = |t_1 - t_2|$, as a function of $|t_1 - t_2| = \Delta/2$. At small Δ , the error extrapolates to a single linear slope almost independent of L . At larger Δ , by contrast, there is a large L dependence, and there seems to be a crossover between the two regions.

In Fig. 14(c), we plotted the error [cross section of Fig. 14(b)] for fixed $\mu = \Delta/2$ as a function of $1/L$ in the intermediate region, and as a function of $1/L^2$ at large- Δ region. From these results, one could anticipate the following systematic behavior: at $\Delta \lesssim 4/L$, the error is an L -independent constant, only depending linearly on Δ . With increasing Δ , they start to show a $1/L$ dependence, and finally at large Δ , the error crossovers to the $1/L^2$ -dependent one. This behavior is nothing but the normal one generally found in the finite size scaling analysis. Thus, the gapped region (plateau structure) is extracted by systematically analyzing the $\mu - \langle n_{L/2} \rangle$ dependence in large systems. Even when L is rather small, one can roughly estimate the size of the gap from the L dependence of the $\mu - \langle n_{L/2} \rangle$ curve as shown in Fig. 14(a).

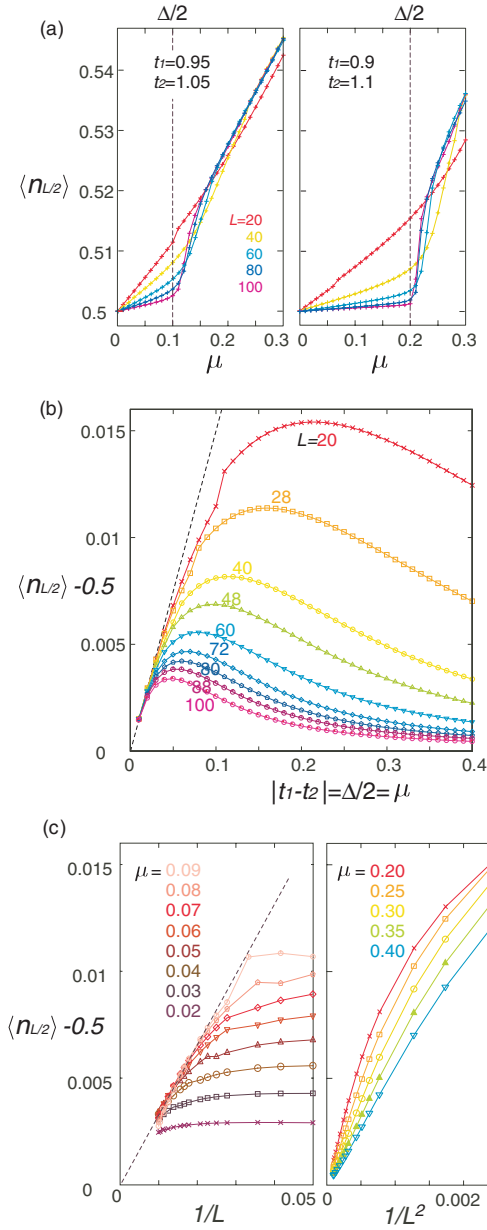


FIG. 14. (Color online) (a) μ dependence of the particle density at the center of the system in the noninteracting t_1 - t_2 model, with $t_1 - t_2 = 0.1$ (left panel) and 0.2 (right panel). (b) Errors of $\langle n_{L/2} \rangle$ from the exact particle density ($=0.5$) at $\mu = |t_1 - t_2| = \Delta/2$, namely, at the opening of a gap indicated by dotted line in (a), examined under the variation of Δ as well as L . (c) Error in (b) (several cross sections at fixed μ) when $\Delta/2 \lesssim 0.1$ (left panel) and $\Delta/2 \gtrsim 0.2$ (right panel), as functions of $1/L$ and $1/L^2$, respectively.

Figure 15 show the results of the grand canonical analysis of the Hubbard model

$$\mathcal{H} = \sum_{j=1}^{L-1} \sum_{\sigma} \left(c_{j\sigma}^{\dagger} c_{j+1\sigma} + \text{H.c.} \right) + \sum_{j=1}^L U \left(n_{j\uparrow} - \frac{1}{2} \right) \left(n_{j\downarrow} - \frac{1}{2} \right). \quad (\text{A2})$$

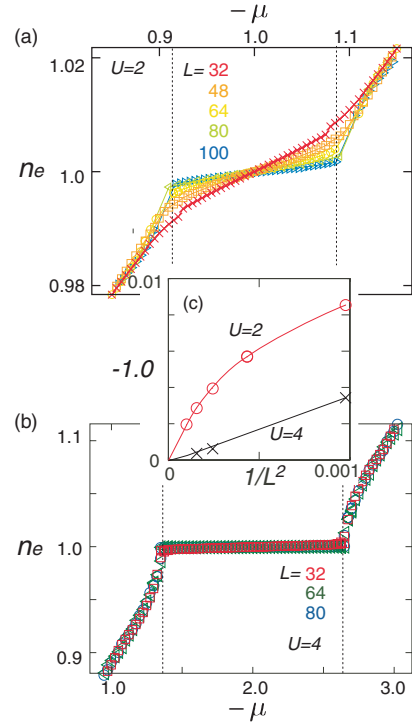


FIG. 15. (Color online) Results (μ - n_e curve) of the grand canonical analysis on the Hubbard model at (a) $U = 2$ and (b) $U = 4$. The broken line indicates the location of a gap obtained by the exact solution. The error at the opening of a gap in (a) and (b) is summarized in (c) as a function of $1/L^2$.

The results of $U = 2$ and 4 are compared. In the former case in Fig. 15(a), where $\Delta < O(1/10)$, the in-gap error follows those of the left panel in Fig. 14(c), the intermediate region with an error linear to $1/L$. The latter case shows a $1/L^2$ dependence of error, corresponding to the right panel of Fig. 14(c), the large- Δ region. Thus, the systematic behavior of the in-gap error we found for the noninteracting fermions is reproduced in the interacting electronic system. Here, notice that even though the plateau has a curve due to the large error, the crossing point of the plateau with the upper and lower curves is hardly influenced by this error. Thus, one could give a relatively reliable evaluation of the range of the plateau.

APPENDIX B: NON-SSD DEFORMATION

Now, let us discuss what happens if we consider the other type of deformation instead of SSD. For example, one could come up with the deformation which has a stepwise structure. This type of deformation is indeed studied in the early stage by Vekic and White^{32,33} as a so-called “smooth boundary condition.” We applied several different types of deformation function to the $S = \frac{1}{2}$ Heisenberg model whose Hamiltonian is given in Eq. (27).

Figures 16(a) and 16(b) show spatial profiles of the local magnetization density $\langle S_i^z \rangle$ in an applied magnetic field $h = 1$, with the Fermi distribution functionlike $f(j)$ and with the power function, respectively (see the insets). One finds that as the step of $f(x)$ becomes steep, the larger the oscillations become. The corresponding $O(r)$ measured from the exact

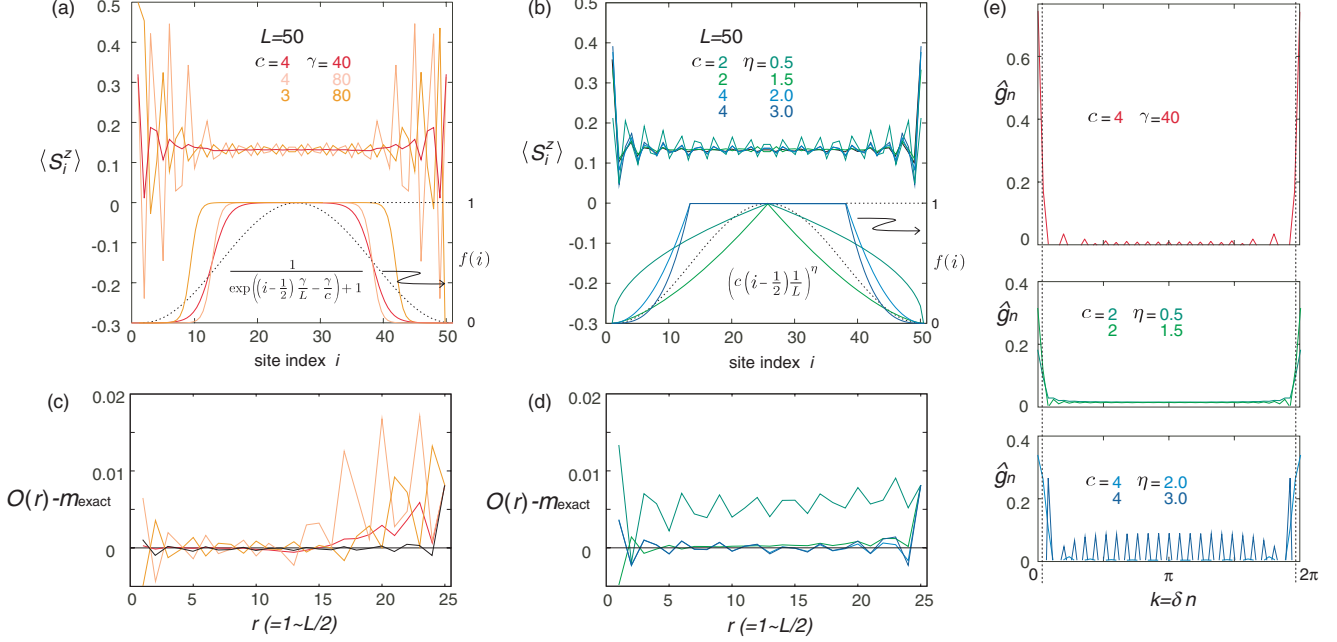


FIG. 16. (Color online) The results of the $S = \frac{1}{2}$ 1D Heisenberg model in an applied field $h = 1$ by DMRG in a grand canonical analysis (to be compared with the SSD ones in Fig. 10.) Several (a) step functions and (b) power functions shown in the inset are applied. Their k -Fourier components of $\hat{g}(k)$ in Eq. (14) are given in (e). (c) and (d) are $O(r)$ in Eq. (10) measured from the exact result.

solution is given in Figs. 16(c) and 16(d). The fitting shall give relatively reasonable results overall, even though the oscillation is present. However, for the $c = 2, \eta = 0.5$ power function, which does not have enough zero energy range in real space near the edges, fails to give a proper $O(r)$; it deviates by several orders of magnitude than others from the exact result.

The profiles of \hat{g}_n [the Fourier component of $g(j) = 1 - f(j)$] are given in Fig. 16(e): few of them have a relatively large amplitude at $k = \delta$, i.e., $(c, \gamma) = (4, 40), (2, 1.5), (4, 3)$. These functions are quite successful in the analysis compared to other functions [see Figs. 16(a)–16(d)]. This could be understood by reminding that the SSD function had a delta-functional peak in \hat{g}_k at $k = \delta$, and by recalling the discussions in Sec. III; the shape of $g(j)$, which is the most smoothly varying one, covering the whole system exactly by the single wavelength, should mix the eigenstates ψ_k between nearest neighbor k 's and gives the optimal reconstruction of the energy level (namely, SSD or SSD-like functions). As the step becomes steeper, the results become worse, indicating that steep function is not preferred. The small $\hat{g}(k)$ components distributing in the intermediate k points seem to rumple the wave function by mixing the k and $k + dk$ of large intervals, giving rise to the oscillation, but its artifact itself is not severe. Whereas, a large peak at $k = 0$, which contributes to the diagonal element of the Hamiltonian, relatively weakens the effect of off-diagonal mixing by $\hat{g}(k = \delta)$, which hinders the generation of good edge states. We also note that, even though some of these functions presented here could finally give a reasonable result, the convergence of the variational calculation (DMRG) is several times slower than the SSD case, particularly when we adopt the steplike function. We again argue that the SSD function is the optimal function for the grand canonical analysis.

APPENDIX C: NONINTERACTING FERMIONS ON TWO-DIMENSIONAL LATTICES

The analysis similar to that given in Sec. III for the 1D noninteracting fermionic system is presented here for the 2D lattices. We show the results for the noninteracting tight-binding fermions on a series of clusters in units of square and triangle in Figs. 1(c)–1(e), which are characterized by the total number of sites N . We first apply two types of deformation, the Cartesian SSD in Eq. (4) and the polar SSD in Eq. (5), for a square lattice. The former deformation is already introduced by Maruyama *et al.*⁷ where they tried to recover the wave function of the PBC as explained in Sec. III B; they found that in 2D, even a fine tuned μ still yields an edge state and can not fully recover the PBC wave function, in contrast to the 1D case. This is because the relation to fully suppress the mixing between states below and above zero energy $\mu = -2[\cos(k_x \pm \delta/2) + \cos(k_y \pm \delta/2)]$ can not be completed for all choices of (k_x, k_y) due to the misfit of the geometry of discrete k meshes and the shape of the Fermi surface. But, this fact does not matter in our analysis.

Figure 17(a) shows the spatial profile of particle number $\langle n(x, y) \rangle$ on the $y = 0.5$ cut of the $L = 10$ ($N = L \times L = 100$) cluster in Fig. 1(b) for several choices of μ . Although the lattice length is as small as $L = 10$, the deformation works quite well, and n_e near the center systematically varies with μ . Figures 17(b) and 17(c) show $\langle n(1/2, 1/2) \rangle = \langle n_{\text{center}} \rangle$ and $\langle n_{\text{center}} \rangle - n_{\text{exact}}$, respectively, as functions of μ . At $L \gtrsim 10$, the error is suppressed to less than 10^{-3} .

The same operation is done for the polar SSD. Figures 17(e)–17(g) are results corresponding to Figs. 17(b)–17(d). Here, we take $R = 2, 3.5, 4.5, 6$ for $L = 4, 6, 8, 10$,

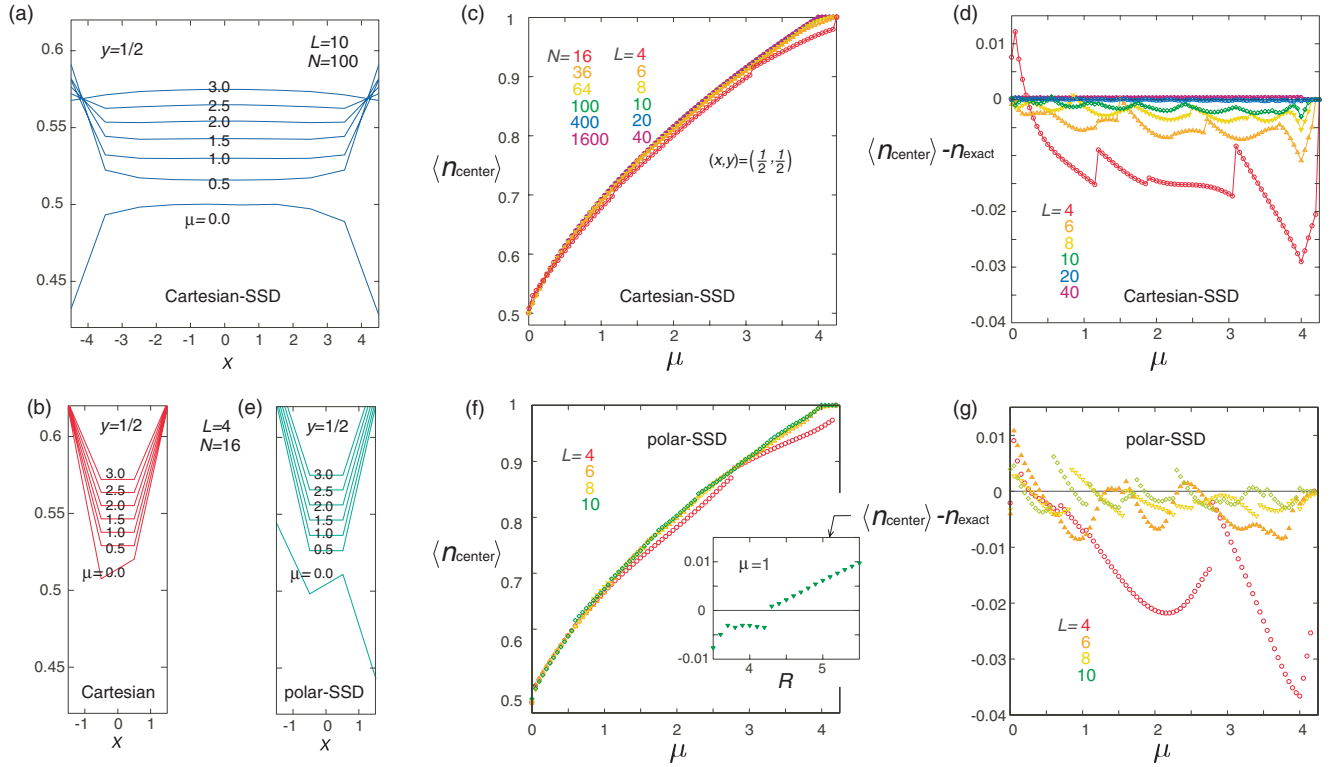


FIG. 17. (Color online) Results of the noninteracting fermions on a square lattice in Fig. 1(b) by the SSD deformation. Spatial distribution of $\langle n(x,y) \rangle$ of (a) $L = 10$ and (b) $L = 4$, (c) $\langle n(1/2, 1/2) \rangle$ [denoted as n_{center} for a series of clusters with $L = 4, 6, 8, 10$ ($N = L \times L$)], and (d) the corresponding errors $\langle n_{\text{center}} \rangle - n_{\text{exact}}$, as functions of μ from half-filling to the fully occupied level for the Cartesian SSD. Panels (e), (f), and (g) are the corresponding results of (b), (c), and (d) for the polar SSD. The inset of panel (f) shows the R dependence of $n_{\text{center}} - n_{\text{exact}}$ for $L = 10, \mu = 1$.

which are approximately the maximum distance to the edge sites measured from the center. By comparing the errors, one finds that the accuracy remains within the same order, i.e., the way of deformation does not influence the accuracy much. We also examined the R dependence of accuracy. As shown in the inset of Fig. 17(f), the best accuracy is obtained at around $R \sim L/\sqrt{2}$, which is the radius that exactly covers the whole cluster as indicated by circles in Fig. 1(b). This also supports

our discussion in the previous section: $f(r)$ made up of a single wave of length $2R$ gives the optimal results.

The polar deformation is given for two different types of triangular lattice clusters as well. As shown in Figs. 18(a)–18(c), the typical error of n_{center} is suppressed to the order of 10^{-3} once $2R \gtrsim 10$. As is well known, the density of states of the triangular lattice tight-binding model has a van Hove singularity at $\mu = 2$, which corresponds to the divergence of

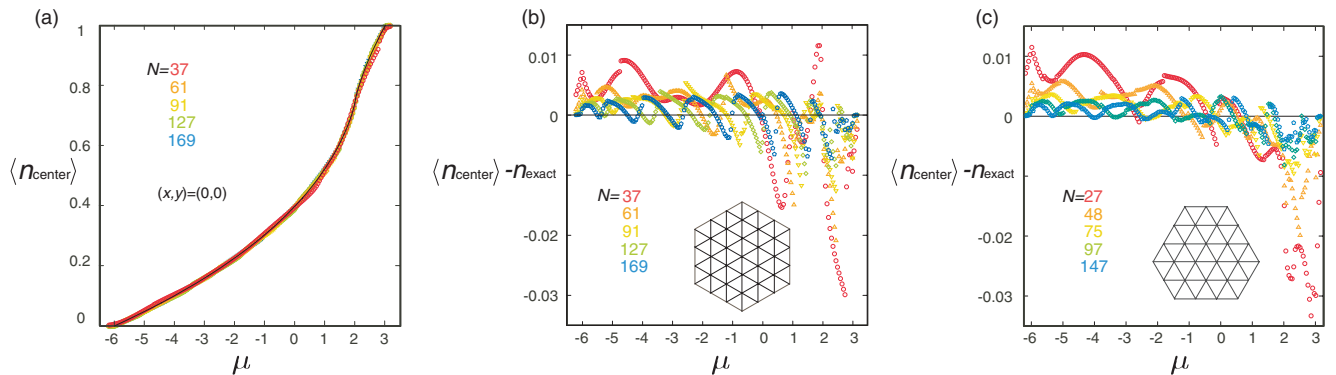


FIG. 18. (Color online) Results of the noninteracting fermions on a triangular lattice, on a hexagonal cluster (a), (b) [Fig. 1(c)], and irregular hexagonal cluster (c) [Fig. 1(d)] by the polar SSD deformation, where we take R as the half-integer or integer number closest to the radius of the minimum circle which covers the whole cluster. Particle density $\langle n_{\text{center}} \rangle$ and its error $\langle n_{\text{center}} \rangle - n_{\text{exact}}$ at the center of the cluster [for (a), (b) we take the center site, and for (c) we take the vertex of the center triangle] as functions of μ over the whole energy band. Solid line in panel (a) represents n_{exact} .

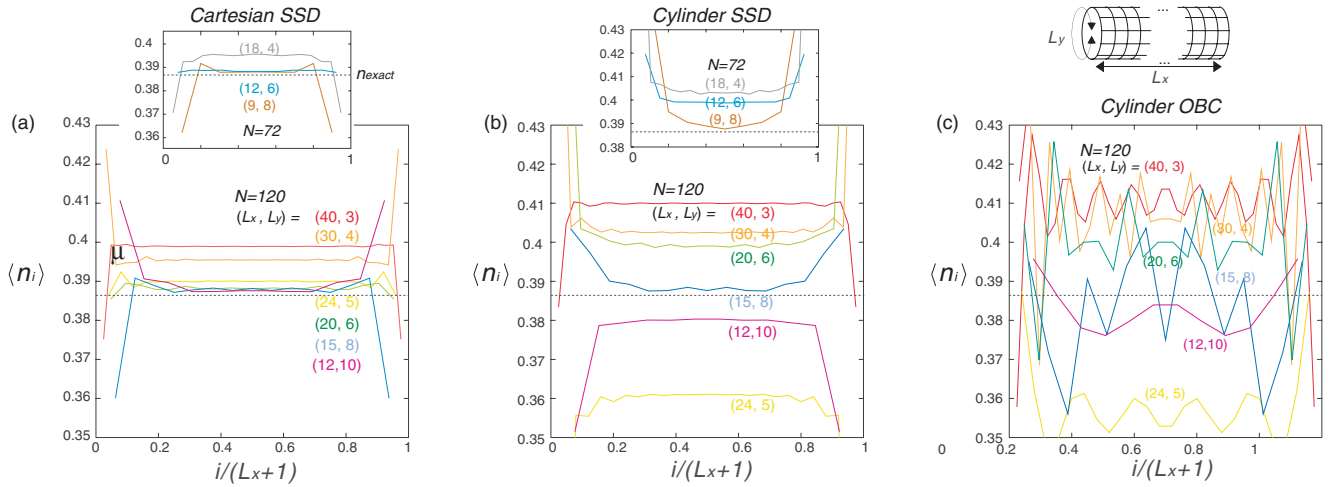


FIG. 19. (Color online) Examination of the effect of the aspect ratio on the particle density of the noninteracting fermions. On the $N = L_x \times L_y$ rectangular cluster ($L_x > L_y$), we compare three different types of deformation: (a) Cartesian SSD deformation by Eq. (4), (b) cylinder deformation by Eq. (3) along the x direction, and (c) cylinder (nondeformed) with PBC and OBC along the x and y directions, respectively. The profile of the particle density along the x direction is shown for different aspect ratio at fixed $N = 120$ [$N = 72$ in the inset of (a) and (b)] and $\mu = -0.5$. [In (a), $\langle n_i \rangle$ has y dependence so that we take $y = L_y/2$ and $(L_y + 1)/2$ for even and odd L_y , respectively. In cylinders, the y direction is translationally invariant.] Broken line indicates the exact result n_{exact} .

the gradient of n_e . However, such singularity does not seem to influence the accuracy of this analysis.

APPENDIX D: ASPECT RATIO OF THE CLUSTER

In 2D, the shape of the cluster generally influences the results, particularly when the size of the cluster is small. Here, we examine the case of the square lattice spanned on the rectangular cluster $N = L_x \times L_y$ by adopting the Cartesian SSD, cylinder SSD, and the usual OBC cylinder without deformation. Figures 19(a)–19(c) show the spatial profile of the electron density along the x direction $\langle n_i \rangle$ ($i = 1 \sim L_x$) at fixed N for different aspect ratio (L_x/L_y). In the Cartesian case, the value of $\langle n_i \rangle$ at $i = L_x/2$ monotonously converges to the exact value as the aspect ratio approaches unity. Note that if we fix $L_y \lesssim 10$ and increase L_x , the accuracy does not depend on the aspect ratio itself but depends on the shorter sidelength L_y . The cylinder SSD also has a better evaluation for aspect ratio closer to unity, however, $\langle n_i \rangle$ takes the value both below and above n_{exact} depending on the period of the circumference

L_y , and are not systematic. The results of the cylinder OBC have large oscillations due to the boundary effect, but the oscillation center shows similar aspect ratio dependence with results of the cylinder SSD.

Here, the following three conclusions are derived. First, taking the maximum of the available N , and setting the aspect ratio closest to unity (to make the shortest sidelength as large as possible), gives the most reliable “bulk” property. Second, the accuracy of the grand canonical analysis is relatively insensitive to the period of the cluster as far it is deformed. Finally, the results of the cylinder SSD, although better than the cylinder OBC, depend much on the lattice period along the circumference, and are much less reliable.

Thus, if the available system size is limited, it is better to have N spanned on a cluster with an aspect ratio closest to unity, and deform it in all directions (polar SSD is also fine). Although cylinders sometimes provide us with better numerical accuracy, they may not show systematic dependence of physical quantities both on the aspect ratio and on the sidelength.

¹N. Shibata and C. Hotta, *Phys. Rev. B* **84**, 115116 (2011).

²C. L. Kane and E. J. Mele, *Phys. Rev. Lett.* **95**, 226801 (2005).

³C. Hotta and N. Shibata, *Phys. Rev. B* **86**, 041108(R) (2012).

⁴K. G. Wilson, *Rev. Mod. Phys.* **4**, 773 (1975).

⁵S. R. White, *Phys. Rev. Lett.* **69**, 2863 (1992).

⁶A. Gendiar, M. Daniska, Y. Lee, and T. Nishino, *Phys. Rev. A* **83**, 052118 (2011).

⁷I. Maruyama, H. Katsura, and T. Hikiyara, *Phys. Rev. B* **84**, 165132 (2011).

⁸The SSD function in Ref. 7 is the same as Eq. (3). Whereas, in Eq. (16), we renormalized the function by a factor of 2 to

conveniently adopt to Eq. (13). The normalization factor of $f(j)$ could be chosen arbitrarily in general.

⁹In practice, the wave number k is still not a good quantum number of \mathcal{H}_{SSD} because the one-particle states below the Fermi level still mix by \mathcal{H}_d , and form another set of wave functions $\Phi_{\text{SSD}} = \prod_l [\sum_j \varphi_l(j)^* c_j^\dagger] |0\rangle$. Whereas, the bases $c_j^\dagger |0\rangle$ and $c_k^\dagger |0\rangle$ are in one-to-one correspondence by the unitary transformation, thus, Φ_{SSD} is reproduced exactly from Ψ_{PBC} .

¹⁰H. Katsura, *J. Phys. A: Math. Theor.* **44**, 252001 (2011).

¹¹H. Katsura, *J. Phys. A: Math. Theor.* **45**, 115003 (2012).

¹²T. Hikiyara and T. Nishino, *Phys. Rev. B* **83**, 060414(R) (2011).

- ¹³A. Gendiar, R. Kremer, and T. Nishino, *Prog. Theor. Phys.* **122**, 953 (2009); **123**, 393 (2010).
- ¹⁴The $1/L^2$ dependence of SSD energy levels is also pointed out by H. Katsura (private communication).
- ¹⁵K. Okunishi and T. Nishino, *Phys. Rev. B* **82**, 144409 (2010).
- ¹⁶See the following articles and the references therein, U. Schollöck, *Rev. Mod. Phys.* **77**, 259 (2005).
- ¹⁷Weihong Zheng, J. Oitmaa, and C. J. Hamer, *Phys. Rev. B* **43**, 8321 (1991).
- ¹⁸C. J. Hamer, Weihong Zheng, and P. Arndt, *Phys. Rev. B* **46**, 6276 (1992).
- ¹⁹M. E. Zhitomirsky and T. Nikuni, *Phys. Rev. B* **57**, 5013 (1998).
- ²⁰A. Honecker, *J. Phys.: Condens. Matter* **11**, 4697 (1999).
- ²¹H. Nishimori and S. Miyashita, *J. Phys. Soc. Jpn.* **55**, 4448 (1986).
- ²²T. Sakai and H. Nakano, *Phys. Rev. B* **83**, 100405(R) (2011).
- ²³A. V. Chubukov and D. I. Golosov, *J. Phys.: Condens. Matter* **3**, 69 (1991).
- ²⁴D. J. J. Farnell, R. Zinke, J. Schulenburg, and J. Richter, *J. Phys.: Condens. Matter* **21**, 406002 (2009).
- ²⁵A. W. Sandvik, *Phys. Rev. B* **85**, 134407 (2012).
- ²⁶S. Nishimoto, S.-L. Drechsler, R. O. Kuzian, J. van den Brink, J. Richter, W. E. A. Lorenz, Y. Skourski, R. Klingeler, and B. Büchner, *Phys. Rev. Lett.* **107**, 097201 (2011).
- ²⁷S. R. White and A. L. Chernyshev, *Phys. Rev. Lett.* **99**, 127004 (2007).
- ²⁸R. Coldea, D. A. Tennant, A. M. Tsvelik, and Z. Tylczynski, *Phys. Rev. Lett.* **86**, 1335 (2001).
- ²⁹T. Ono, H. Tanaka, H. Aruga Katori, F. Ishikawa, H. Mitamura, and T. Goto, *Phys. Rev. B* **67**, 104431 (2003).
- ³⁰N. A. Fortune, S. T. Hannahs, Y. Yoshida, T. E. Sherline, T. Ono, H. Tanaka, and Y. Takano, *Phys. Rev. Lett.* **102**, 257201 (2009).
- ³¹Y. Shirata, H. Tanaka, A. Matsuo, and K. Kindo, *Phys. Rev. Lett.* **108**, 057205 (2012).
- ³²M. Vekić and S. R. White, *Phys. Rev. Lett.* **71**, 4283 (1993).
- ³³M. Vekić and S. R. White, *Phys. Rev. B* **53**, 14552 (1996).